The microbiota regulate neuronal function and fear extinction learning

https://doi.org/10.1038/s41586-019-1644-y

Received: 23 August 2018

Accepted: 5 September 2019

Coco Chu[1], Mitchell H. Murdock[2,3,4], Deqiang Jing[3,4,5], Tae Hyung Won[6], Hattie Chung[7], Adam M. Kressel[8,9,10], Tea Tsaava[8], Meghan E. Addorisio[8], Gregory G. Putzel[1], Lei Zhou[1], Nicholas J. Bessman[1], Ruirong Yang[3,4,5], Saya Moriyama[1], Christopher N. Parkhurst[1], Anfei Li[3,4], Heidi C. Meyer[3], Fei Teng[1], Sangeeta S. Chavan[8,9,11], Kevin J. Tracey[8,9,11], Aviv Regev[7,12], Frank C. Schroeder[6], Francis S. Lee[3,4,5], Conor Liston[2,3,4]* & David Artis[1,13]*

Multicellular organisms have co-evolved with complex consortia of viruses, bacteria, fungi and parasites, collectively referred to as the microbiota[1]. In mammals, changes in the composition of the microbiota can influence many physiologic processes (including development, metabolism and immune cell function) and are associated with susceptibility to multiple diseases[2]. Alterations in the microbiota can also modulate host behaviours—such as social activity, stress, and anxiety-related responses—that are linked to diverse neuropsychiatric disorders[3]. However, the mechanisms by which the microbiota influence neuronal activity and host behaviour remain poorly defined. Here we show that manipulation of the microbiota in antibiotic-treated or germ-free adult mice results in significant deficits in fear extinction learning. Single-nucleus RNA sequencing of the medial prefrontal cortex of the brain revealed significant alterations in gene expression in excitatory neurons, glia and other cell types. Transcranial two-photon imaging showed that deficits in extinction learning after manipulation of the microbiota in adult mice were associated with defective learning-related remodelling of postsynaptic dendritic spines and reduced activity in cue-encoding neurons in the medial prefrontal cortex. In addition, selective re-establishment of the microbiota revealed a limited neonatal developmental window in which microbiota-derived signals can restore normal extinction learning in adulthood. Finally, unbiased metabolomic analysis identified four metabolites that were significantly downregulated in germ-free mice and have been reported to be related to neuropsychiatric disorders in humans and mouse models, suggesting that microbiota-derived compounds may directly affect brain function and behaviour. Together, these data indicate that fear extinction learning requires microbiota-derived signals both during early postnatal neurodevelopment and in adult mice, with implications for our understanding of how diet, infection, and lifestyle influence brain health and subsequent susceptibility to neuropsychiatric disorders.

Pavlovian fear conditioning is an evolutionarily conserved associative learning process that is critical for the survival of an organism and for the ability to respond appropriately to neutral stimuli that reliably predict dangerous or aversive outcomes[4]. In the classical fear conditioning paradigm, extinction learning occurs when repeated cue presentations are no longer paired with an unconditioned stimulus (such as a foot shock) and the organism learns to modify its behaviour accordingly. Deficits in extinction learning after an environmental threat has passed have been implicated in multiple neuropsychiatric disorders, including post-traumatic stress disorder and other anxiety disorders[5]. Clinical and epidemiological studies have reported correlations between changes in the microbiota and other neuropsychiatric disorders[6–8]. Animal studies indicate that the absence or modification of the intestinal microbiota affects neurogenesis[9], cortical myelination[10], the function of the blood–brain barrier[11] and maturation of microglia[12], as well as social behaviour, stress-related responses and fear learning[3,13,14]. However, there are conflicting reports on how the microbiota influence behaviour[13–16], and the mechanisms through which the microbiota regulate associative learning and its neurobiological substrates remain unclear.

Lack of microbiota impairs extinction learning

To test whether the microbiota influence fear conditioning and extinction, we first treated adult mice with antibiotics (termed ABX mice)[17] and used a classical cued fear conditioning and extinction learning paradigm[18]. ABX mice and control mice showed comparable food and

---

A list of affiliations appears at the end of the paper.

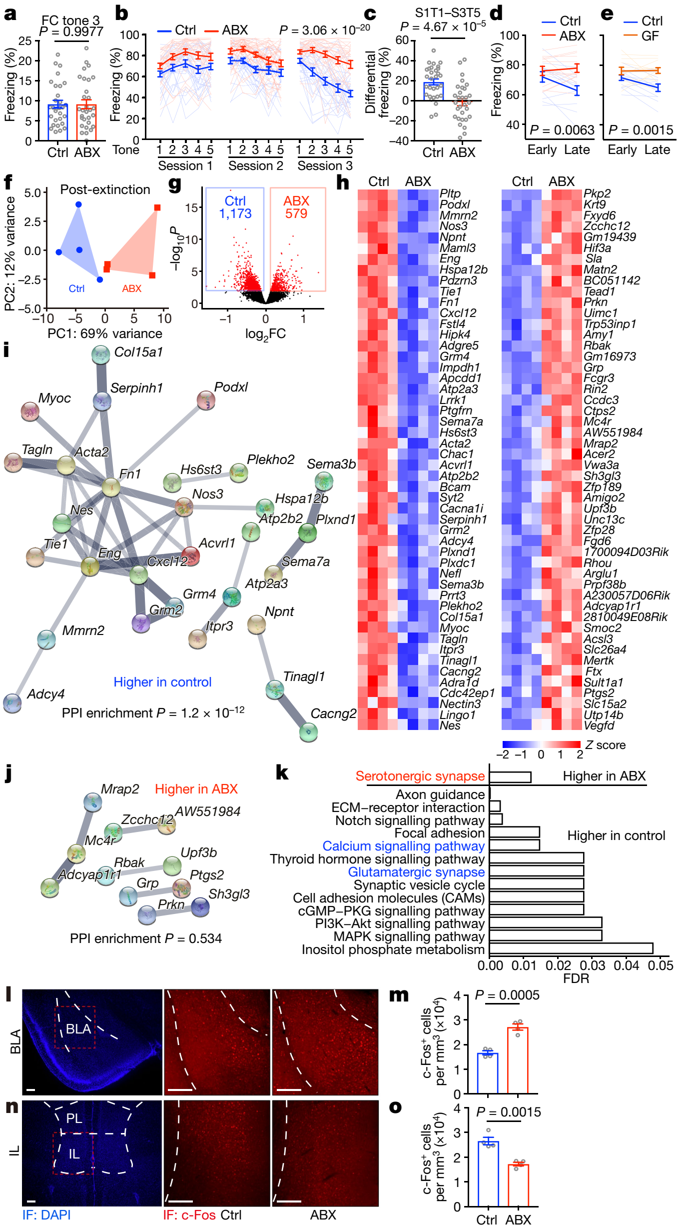

Fig. 1 | ABX and GF mice are less prone to fear extinction. a–c, Acquisition of fear conditioning (FC) (**a**), fear extinction over the course of three days or sessions (**b**) and fear conditioning after three days (**c**) in control (Ctrl) and ABX mice. S, session; T, tone. Data pooled from two independent experiments. $n = 30$ mice per group. Mean ± s.e.m.; unpaired two-sided *t*-test (**a**, **c**); for **b**, area under the curve (AUC) was calculated for each mouse within each group followed by unpaired two-sided *t*-test between groups. **d**, **e**, Fear extinction in control versus ABX (**d**) or control versus GF (**e**) mice in the single-session 30-tone fear extinction assay. Data pooled from two independent experiments, $n = 12$ mice per group. Mean ± s.e.m.; the AUC was calculated for each mouse within each group followed by unpaired two-sided *t*-test between groups. **f**, Principle component analysis (PCA) of mouse mPFC transcriptome after fear extinction. $n = 4$ mice per group. Permutational multivariate analysis of variance (PERMANOVA): $F = 5.00$, Df = 1, $P = 0.027$. **g**, Volcano plot of differential expression of genes in ABX versus control groups in **f**. Red dots, differentially expressed genes (DESeq2 Wald test, false discovery rate (FDR) < 0.1). FC, fold change. **h**, Heat maps showing the top 50 most significantly downregulated or upregulated genes in **g**. Low-expression genes with mean normalized counts in the bottom 20th percentile were excluded. **i**, **j**, STRING network visualization of the genes in **h**. Edges represent protein–protein associations. Disconnected nodes were excluded. **k**, Significantly enriched KEGG pathways based on all differentially expressed genes in **g**. **l**–**o**, Immunofluorescence (IF) staining (**l**, **n**) and the density of c-FOS$^+$ neurons (**m**, **o**) in the BLA (**l**, **m**) or IL (**n**, **o**) of control and ABX mice after fear extinction session 3. Data are representative of two independent experiments. $n = 4$ mice per group. Mean ± s.e.m.; unpaired two-sided *t*-test. PL, prelimbic. Scale bar, 200 μm.

water intake and weight gain (Extended Data Fig. 1a–c). The bacterial burden was 600-fold lower in ABX mice than in control mice (Extended Data Fig. 1d), and 16S ribosomal DNA (rDNA) sequencing revealed an antibiotic-induced shift in bacterial community structure (Extended Data Fig. 1e–g). Following fear conditioning, ABX mice displayed equivalent freezing behaviour to control mice, indicating that their acquisition of fear conditioning was normal (Fig. 1a). Extinction learning reduced conditioned freezing in control mice[18]. By contrast, extinction learning was significantly impaired in ABX mice (Fig. 1b, c). To further examine the influence of the microbiota on extinction learning, we performed a similar cued fear conditioning and extinction learning assay in adult germ-free (GF) mice. To maintain the microorganism-free status of the GF mice, we used a modified single-session fear extinction protocol[19]. Again, both ABX and GF mice exhibited impaired extinction learning (Fig. 1d, e). These data show that signals derived from the microbiota are necessary for optimal extinction of conditioned fear responses.

The vagus nerve is one route of neuronal communication between the intestine and the brain[20,21]. We investigated whether the vagus nerve is involved in extinction learning deficits following manipulation of the microbiota by carrying out surgical vagotomy on adult mice. Vagotomized ABX mice exhibited similar deficits in extinction learning to sham-operated ABX mice, suggesting that the extinction learning deficits in ABX mice are independent of the vagus nerve (Extended Data Fig. 2).

Given that microbiota-derived signals can regulate the immune system and that immune cells can influence brain function and behaviour[22–24], we tested whether the extinction learning deficits were associated with alterations in immune responses in the brain. Compared to control mice, ABX and GF mice showed no differences in the percentages and numbers of CD45^{high} leukocytes in the brain (Extended Data Fig. 3a, b, e), and no differences in the percentages of CD4$^+$ T cells, CD8$^+$ T cells, CD19$^+$ B cells, CD11c$^+$ dendritic cells, F4/80$^+$ macrophages or Ly6C^{high} monocytes (Extended Data Fig. 3c, d, f–j). Moreover, *Rag1*$^{-/-}$ mice, which lack adaptive immune cells, exhibited normal extinction learning (Extended Data Fig. 3k), whereas GF *Rag1*$^{-/-}$ mice showed deficits in extinction learning (Extended Data Fig. 3l), indicating that the adaptive immune system is not required for extinction learning deficits in ABX and GF mice.

Given that deficits in extinction learning appear to occur independently of changes in the immune system, we investigated their neuroanatomical basis. We performed genome-wide transcriptional profiling of the medial prefrontal cortex (mPFC), an area of the brain known to be crucial for extinction learning[25], from adult ABX and control mice. mPFC tissue dissected from adult ABX and control mice that had not undergone fear conditioning and extinction exhibited comparable transcriptomes (Extended Data Fig. 4a, b). However, extinction learning led to significant differences in the transcriptomes of mPFC tissue from ABX and control mice (Fig. 1f, g). Search tool for recurring instances of neighbouring genes (STRING) analysis depicted networks of interactions of the differentially expressed genes (DEGs) between ABX and control samples (Fig. 1h–j); Kyoto Encyclopedia of Genes and Genomes (KEGG) and Gene Ontology (GO) enrichment analyses identified pathways that are associated with neuronal activity, synapse function, CNS maturation and the regulation of synaptic plasticity and the development of postsynaptic dendritic spines (Fig. 1k, Supplementary Table 1).

To test whether alterations in gene expression associated with these neuronal processes were associated with changes in neuronal activity, we examined neuronal activity in fear learning circuits by analysing c-FOS expression[26] in the basolateral amygdala (BLA), which is critical for encoding and storing conditioned fear memory[27], and in the infralimbic region (IL) of the mPFC, which facilitates extinction learning[25].

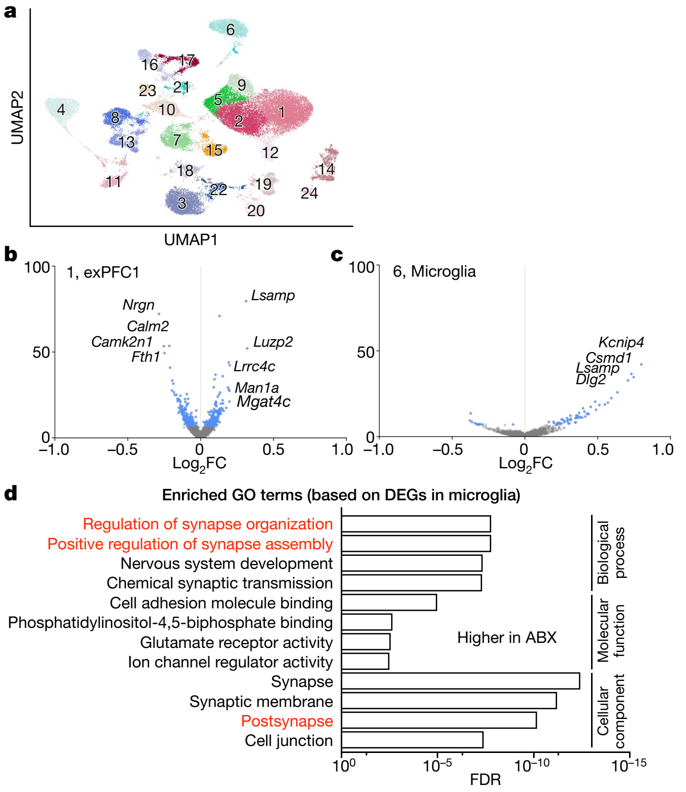

Fig. 2 | Excitatory neurons and microglia are affected in ABX mice. a, Single nucleus profiles coloured by cell type (see Extended Data Fig. 5 for annotations). $n = 2$ mice per group. **b**, **c**, Differentially expressed genes (blue dots: z-test calculated on coefficients of mixed linear model, Bonferroni-corrected $P < 10^{-7}$) of ABX versus control in excitatory neuron subset 1 (exPFC1, **b**) or 6 (microglia, **c**). **d**, GO terms that were significantly enriched among the differentially expressed genes in the microglial cluster in **c**.

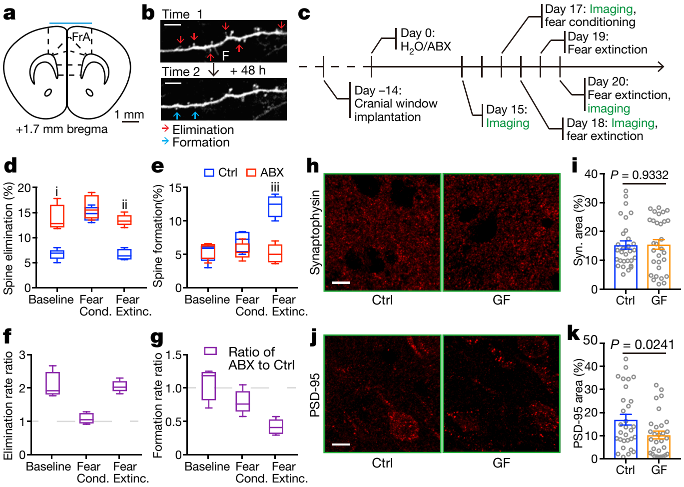

Fig. 3 | Defective extinction-learning-related dendritic spine formation in ABX mice. a, Diagrammatic representation of a coronal section of the mPFC showing the imaging site (cyan bar). FrA, frontal association cortex. **b**, Example images of neuronal dendritic branch segments at two consecutive imaging time points. Red arrows, spine elimination. Blue arrows, spine formation. Scale bar, 5 µm. F, filopodia. **c**, Timeline of transcranial two-photon spine imaging. **d**, **e**, Percentage of spine elimination (**d**) and formation (**e**) at baseline, during fear conditioning and during fear extinction. **f**, **g**, Ratio of ABX to control for spine elimination rate (**f**) and spine formation rate (**g**). Data in **d**–**g** are pooled from three independent experiments. $n = 5$ mice per group. Centre line, median; box, 25th and 75th percentiles; whiskers, minimum to maximum. Unpaired two-sided t-tests were used in **d**, **e**. i, $P = 0.0010$; ii, $P = 4.38 \times 10^{-5}$; iii, $P = 0.0002$. **h**–**k**, Immunofluorescence staining and the area of synaptophysin (**h**, **i**) or PSD-95 (**i**, **k**) in the mPFC of control and GF mice. Data are pooled from two independent experiments. $n = 6$ mice per group. Each symbol represents one region of interest (ROI); five ROIs per mouse. Mean ± s.e.m.; unpaired two-sided t-test. Scale bars, 10 µm.

Compared to control mice, ABX and GF mice exhibited a higher density of c-FOS$^+$ neurons in the BLA (Fig. 1l, m, Extended Data Fig. 4c, d) and lower density of c-FOS$^+$ neurons in the IL (Fig. 1n, o, Extended Data Fig. 4e, f), which is consistent with their deficits in extinction learning.

Neuronal and glial changes in ABX mice

To define the cell subsets in the mPFC that contribute to the effect of the microbiota on extinction learning, we performed single-nucleus RNA sequencing (snRNA-seq) of mPFC samples dissected from ABX and control mice after extinction learning, and identified 24 cell clusters (Fig. 2a, Extended Data Fig. 5a). Changes in the microbiota were associated with significant changes in gene expression in multiple clusters (Extended Data Fig. 6). Among the neuronal clusters, excitatory neurons (Fig. 2b, Extended Data Fig. 6) were more affected than inhibitory neurons (including PVALB$^+$TAC1$^+$, SST$^+$, VIP$^+$ and NPY$^+$ subsets) (Extended Data Figs. 5b, 6). Astrocytes, myelinating oligodendrocytes and microglia also showed changes in gene expression (Extended Data Fig. 6). DEGs that were shared across subsets of excitatory neurons (Extended Data Fig. 7) and across multiple cell types (Extended Data Fig. 8) were linked to synapse-related pathways and calcium signalling pathways (Supplementary Tables 2, 3), which is consistent with our bulk RNA-seq data (Fig. 1k) and supports a model in which gene expression is altered in brain-resident cells—including specific cell populations such as excitatory neurons and microglia—following manipulation of the microbiota.

Given that microglia are important for maintaining neuronal function and brain health by dynamically regulating synaptic pruning and surveying their local microenvironments, and have been reported to be affected by the microbiota[12,28], we further investigated the DEGs in microglia (Fig. 2c). The microglial DEGs were enriched in pathways related to synapse organization and synapse assembly (Fig. 2d, Supplementary Table 4), suggesting that deliberate manipulation of the microbiota may alter microglia-mediated synaptic pruning. In addition, consistent with the literature[12], we found elevated percentages and numbers of microglia in GF mice, with elevated expression of CSF1R and F4/80 (Extended Data Fig. 9a–d). The percentages and numbers of microglia in ABX mice were not changed, with no changes in CSF1R expression, but F4/80 expression was elevated (Extended Data Fig. 9e–h). CSF1R and F4/80 are strongly developmentally regulated, and their expression decreases during maturation[29]. Together, these data suggest that microglia in GF and ABX mice exhibit an immature state reminiscent of developing juvenile microglia, which may in turn contribute to deficits in extinction learning by disrupting dendritic spine remodelling.

Defective extinction-related spine remodelling

Next, we used two-photon laser scanning microscopy to directly quantify the remodelling of postsynaptic dendritic spines in the mPFC (Fig. 3a) during cued fear conditioning and extinction learning in transgenic THY1–YFP-H reporter mice, which express yellow fluorescent protein in neurons, following manipulation of the microbiota in adulthood. Postsynaptic dendritic spines are membranous protrusions on neuronal dendrites that form primarily excitatory synapses with presynaptic axonal inputs and are dynamically remodelled during learning and development[30–33]. Fear conditioning and extinction learning are correlated with opposing effects on the formation and elimination of dendritic spines in the mPFC[34]. We acquired images of the same dendritic spines during a baseline period, and before and after fear conditioning and extinction learning (Fig. 3b, c). Compared to control mice, baseline spine elimination rates were significantly elevated in ABX mice (Fig. 3d, f), whereas baseline spine formation rates were unaffected (Fig. 3e, g). Consistent with previous findings[34], cued fear conditioning and extinction learning had opposing effects on spine remodelling in control mice. Fear conditioning increased spine elimination rates in control mice (Fig. 3d), such that there was no significant difference in spine elimination or formation rates in the 24 h after conditioning between ABX mice and control mice (Fig. 3d–g). By contrast, extinction-learning-related spine remodelling was significantly altered in ABX mice. Extinction learning increased spine formation rates in control mice but not in ABX mice (Fig. 3e, g), and spine elimination rates remained persistently elevated in ABX mice relative to control mice (Fig. 3d, f).

Consistent with elevated spine elimination in ABX mice, we observed comparable expression of the presynaptic marker synaptophysin but lower expression of the postsynaptic marker PSD-95 in the mPFC of GF mice compared to control mice (Fig. 3h–k). In addition, the expression of *Dlg4* in excitatory neuron subset 1 (exPFC1) was downregulated in samples from ABX mice compared to those from control mice. Together, these data indicate that alterations in the composition of the microbiota are associated with deficits in learning-induced spine plasticity. Notably, plasma corticosterone levels were comparable in control, ABX and GF mice[35] (Extended Data Fig. 10a, b), indicating that the function of the hypothalamic–pituitary–adrenal axis may not be altered and is not a major driver of microbiota-mediated changes in spine remodelling and fear extinction learning.

Defective tone-encoding ensembles in ABX mice

To investigate whether signals derived from the microbiota regulate learning-related neuronal activity in the mPFC, we used two-photon imaging and a genetically encoded calcium sensor (AAV5–hSyn–GCaMP6s) to quantify neuronal activity during extinction learning in control and ABX mice (Fig. 4a–c). We identified mPFC neurons that encoded the conditioned stimulus, and identified two differentially responding functional cell types. One neuronal population (representing 13.5% of all cells) exhibited equivalently reduced activity during tone presentations in both control and ABX mice (Fig. 4d, e). By contrast, a second population (representing 14.9% of all cells) displayed increased activity during tone presentations (Fig. 4f). In this latter population, neuronal activity during tone presentations was modestly but significantly lower in ABX mice than in control mice (Fig. 4g), consistent with the deficits in spine formation and behaviour in ABX mice. Notably, 26.8% of these neurons also encoded the precise timing of the tones, exhibiting tone-locked activity that increased and decreased in response to the onset and offset of each tone, respectively (Fig. 4h). Again, tone-locked activity in these multicellular tone-sensitive ensembles was significantly reduced in ABX mice compared to control mice (Fig. 4i). In conjunction with the RNA-seq and dendritic spine remodelling analyses, these data indicate that dysbiosis of the gut microbiota disrupts learning-related spine formation and interferes with the emergence of multicellular tone-encoding ensembles.

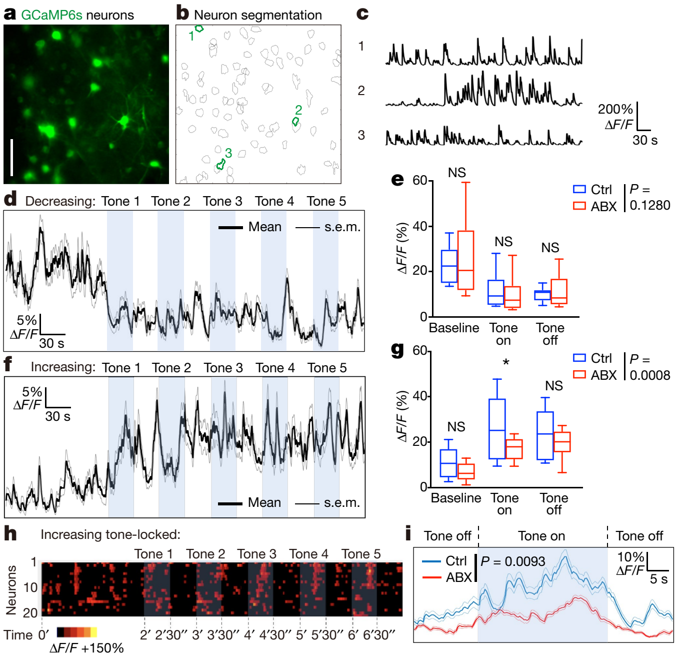

Fig. 4 | Defective ensemble calcium dynamics in the mPFC of ABX mice. **a**, Example false-colour image (mean projection over time) of GCaMP6s-expressing neurons in the mPFC. Scale bar, 50 μm. **b**, Segmentation of the neurons in **a**. **c**, Neuronal activity ($\Delta F/F$) extracted from the three example neurons outlined in **b**. **d**–**g**, Population activity traces (mean $\Delta F/F$ ± s.e.m.) for neurons exhibiting decreased (**d**) or increased (**f**) activity during tone presentations in fear extinction session 3. Mean activity ($\Delta F/F$) during each task epoch (baseline, tone-on, tone-off; **e**) for the neuronal population depicted in **d** presents a significant decrease in activity (repeated-measures analysis of variance (ANOVA): main effect of time: $F(10,1600) = 3.138$, $P = 0.007$) but no significant difference between groups (group-by-time interaction: $F(10,1600) = 2.736$, $P = 0.1280$). NS, not significant (baseline, 0.285; tone-on, 0.595; tone-off, 0.578). Mean activity ($\Delta F/F$) during each task epoch (**g**) for the neuronal population depicted in **f** presents a significant increase in activity (repeated-measures ANOVA: main effect of time: $F(10,1770) = 4.945$, $P < 0.0001$) and a significant group-by-time interaction ($F(10,1770) = 3.806$, $P = 0.0008$). *$P = 0.013$, significant group difference in post-hoc contrast. NS, not significant (baseline, 0.128; tone-off, 0.601). Centre line, median; box, 25th and 75th percentiles; whiskers, minimum to maximum in **e**, **g**. **h**, Raster plot of neuronal activity for cells that encoded the timing of tones by increasing and decreasing activity in response to tone onset and offset, respectively. Each row represents one neuron. **i**, Population activity trace (mean $\Delta F/F$ ± s.e.m.) for neurons depicted in **h**, timelocked to tone onset and averaged across tones. Repeated-measures ANOVA: main effect of time: $F(179,8234) = 7.033$, $P < 0.0001$; group by time interaction: $F(179,8234) = 2.749$, $P = 0.0093$. Data in **d**–**i** based on 1,204 total cells pooled from 3 independent experiments, from $n = 7$ control mice and $n = 8$ ABX mice.

Diverse microbiota restores extinction learning

To test whether the extinction learning deficits caused by altered microbiota can be rescued by colonization with defined individual microorganisms or consortia of microorganisms, we performed fear conditioning and extinction learning in gnotobiotic mice colonized with bacteria that are known to influence other physiologic processes. Notably, following colonization with segmented filamentous bacterium (SFB)[36], *Clostridium* species[37], *Enterobacter* species[38] or altered Schaedler flora (ASF)[39], these gnotobiotic mice still exhibited impaired extinction learning compared to control mice (Fig. 5a), suggesting that a more diverse microbiota is required for normal extinction learning and fear extinction behaviour.

To investigate whether the extinction learning deficits caused by altered microbiota are reversible, we recolonized previously germ-free (ex-GF) mice with a complete microbiota from healthy control mice at various developmental time points. Both ex-GF mice colonized when they were adults (ex-GF_adult) and ex-GF mice colonized at weaning age (ex-GF_weaning) still displayed impaired fear extinction compared to control mice (Fig. 5b, c), indicating that extinction learning deficits were not reversible in GF mice after weaning. However, when ex-GF mice were colonized immediately after birth by fostering to microbiota-replete specific-pathogen-free (SPF) surrogate mothers (ex-GF_fostered mice), their fear extinction behaviour was comparable to that of control_fostered mice (Fig. 5d), indicating that extinction learning and learning-related plasticity require microbiota-derived signals during a

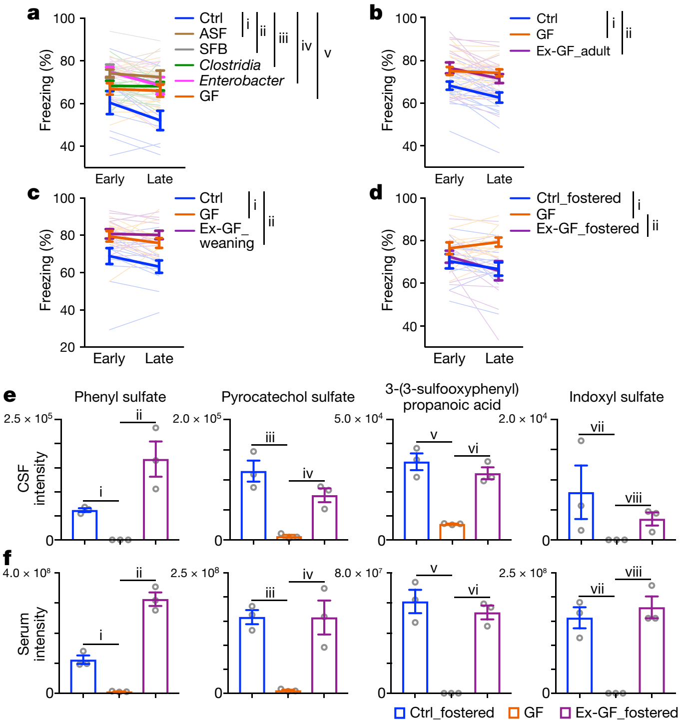

Fig. 5 | Extinction learning deficits in GF mice are associated with alterations in microbiota-derived metabolites. a–**d**, Fear extinction in control, GF and gnotobiotic mice colonized by SFB, *Clostridium*, *Enterobacter* or ASF bacteria (**a**); in control, GF and ex-GF_adult mice (**b**); in control, GF and ex-GF_weaning mice (**c**); or in control, GF and ex-GF_fostered mice (**d**) in the single-session 30-tone fear extinction assay. Data in **a**, **b**, **d** pooled from three independent experiments; data in **c** pooled from two independent experiments. **a**, $n = 9, 13, 9, 12, 7$ and 9 for control, GF, SFB, *Clostridium*, *Enterobacter* and ASF, respectively. **b**, $n = 18$ mice per group. **c**, $n = 12$ mice per group. **d**, $n = 10, 11$ and 12 for Ctrl_fostered, GF, and GF_fostered mice, respectively. Mean ± s.e.m.; AUC calculated for each mouse within each group followed by one-way ANOVA with Tukey's multiple comparisons test. **a**, $F(5,53) = 7.046$, $P = 4.10\times10^{-5}$. Adjusted P values: i, 6.34×10^{-5}; ii, 0.0002; iii, 0.0042; iv, 0.0010; v, 0.0189. **b**, $F(2,51) = 11.92$, $P = 5.66\times10^{-5}$. Adjusted P values: i, 0.0002; ii, 0.0005. **c**, $F(2,33) = 12.64$, $P = 8.40\times10^{-5}$. Adjusted P values: i, 0.0016; ii, 0.0001. **d**, $F(2,30) = 5.131$, $P = 0.0121$. Adjusted P values: i, 0.0228. ii, 0.0273. **e**, **f**, Relative abundances of four compounds in CSF (**e**) and serum (**f**) samples from Ctrl_fostered, GF and GF_fostered mice. $n = 3$ mice per group. Mean ± s.e.m.; unpaired two-sided t-tests were used. **e**, Adjusted P values: i, 9.54×10^{-5}; ii, 0.0102; iii, 0.0036; iv, 0.0044; v, 0.0018; vi, 0.0011; vii, 0.1493; viii, 0.0331. **f**, Adjusted P values: i, 0.0017; ii, 0.0002; iii, 0.0005; iv, 0.0128; v, 0.0014; vi, 0.0003; vii, 0.0020; viii, 0.0014.

critical developmental period before weaning. Lack of the microbiota in the neonatal period, no matter whether microbially colonized or not after weaning, renders deficits in fear extinction learning in adulthood (Fig. 5b–d). Whereas fear extinction was restored in ex-GF_fostered mice, we found no significant shift in the transcriptome of the mPFC of ex-GF_fostered mice or control_fostered mice (compared to GF mice) after the single-session fear extinction training (data not shown). This could reflect the shorter extinction model used in GF mice, which may induce smaller transcriptional changes than the protocol involving one session per day for three days that was used in ABX mice. Alternatively, the lack of transcriptional changes in the GF fostering studies could indicate the involvement of other processes such as post-translational or epigenomic modifications.

Altered CSF metabolites and fear extinction

Next, we investigated whether changes in neuronal development and fear extinction learning were associated with alterations in microbiota-derived metabolites. We used untargeted comparative metabolomics of cerebrospinal fluid (CSF), serum and faecal samples from adult GF mice, control_fostered mice and ex-GF_fostered mice using high-resolution liquid chromatography and mass spectrometry (LC–MS). Using the xcms platform[40] for comparative analysis of the mass spectrometry datasets, we identified four metabolites—phenyl sulfate, pyrocatechol sulfate, 3-(3-sulfooxyphenyl)propanoic acid (all phenolic compounds) and indoxyl sulfate (Extended Data Fig. 10c)—that were significantly decreased in CSF, serum and faecal samples of GF mice compared to control_fostered mice, and were restored in ex-GF_fostered mice (Fig. 5e, f, Extended Data Fig. 10d). Downregulation of the same four metabolites was also detected when we compared GF with control CSF samples (Extended Data Fig. 10e), as well as in comparisons of ABX versus control samples (data not shown). Notably, 3-(3-hydroxyphenyl)-3-hydroxypropanoic acid (HPHPA, a derivative of 3-(3-sulfooxyphenyl) propanoic acid) and indoxyl sulfate have been associated with neuropsychiatric disorders such as impaired executive function, schizophrenia and autism in humans[41–43]. Other microbiota-derived phenolic compounds such as 4-ethylphenylsulfate have been reported to influence autism-related behaviours in mice[44], suggesting that these microbiota-derived compounds may have conserved roles in the development and function of neurons in multiple contexts.

Discussion

This study informs a model in which alterations in exposure to the microbiota in neonatal and adult mice can have considerable and long-lasting effects on neuronal function and learning-related plasticity that subsequently regulate fear extinction behaviour (Extended Data Fig. 10f). From bulk RNA-seq and snRNA-seq data, the deficits in extinction learning correlate with malfunctions of the mPFC, notably in excitatory neurons. Transcranial two-photon live imaging confirmed the changes in neurons in the ABX mice (specifically, reduced extinction learning-associated spine formation and altered learning-related neuronal activity). Given that the vagus nerve does not contribute to the extinction learning deficits in ABX mice in this setting, the microbiota may affect the CNS through circulating microbiota-derived metabolites, directly influencing excitatory neurons in the mPFC and leading to deficits in extinction learning. In addition, microbiota-derived metabolites may also influence other cell subsets in the mPFC (such as microglia), and indirectly affect the excitatory neurons and behaviour. In accordance with this, and consistent with other studies[12], we found that the microglia in GF and ABX mice exhibited an immature state reminiscent of developing juvenile microglia, which may contribute to elevated spine pruning and reduced extinction-learning-associated spine formation. Future studies are necessary to determine the molecular basis of changes to cellular activity in the mPFC induced by alterations in microbiota-derived metabolites.

In summary, our findings offer one compelling explanation for the notable deficits in fear extinction learning in ABX and GF mice, and suggest that alterations in microbiota-derived metabolites contribute to altered neuronal activity and behaviour. Coupled with the growing literature on the influence of the microbiota, diet and lifestyle on chronic inflammatory diseases, metabolic health and cancer, the effects of beneficial microorganisms on brain health and behaviour highlight the need to better define the co-evolved relationship between the microbiota, the nervous system and mammalian behaviour.

Online content

Any methods, additional references, Nature Research reporting summaries, source data, extended data, supplementary information, acknowledgements, peer review information; details of author contributions and competing interests; and statements of data and code availability are available at https://doi.org/10.1038/s41586-019-1644-y.

1. Belkaid, Y. & Hand, T. W. Role of the microbiota in immunity and inflammation. *Cell* **157**, 121–141 (2014).
2. Hill, D. A. & Artis, D. Intestinal bacteria and the regulation of immune cell homeostasis. *Annu. Rev. Immunol*. **28**, 623–667 (2010).
3. Vuong, H. E., Yano, J. M., Fung, T. C. & Hsiao, E. Y. The microbiome and host behavior. *Annu. Rev. Neurosci*. **40**, 21–49 (2017).
4. Maren, S. Neurobiology of Pavlovian fear conditioning. *Annu. Rev. Neurosci*. **24**, 897–931 (2001).
5. VanElzakker, M. B., Dahlgren, M. K., Davis, F. C., Dubois, S. & Shin, L. M. From Pavlov to PTSD: the extinction of conditioned fear in rodents, humans, and anxiety disorders. *Neurobiol. Learn. Mem*. **113**, 3–18 (2014).
6. Mielcarz, D. W. & Kasper, L. H. The gut microbiome in multiple sclerosis. *Curr. Treat. Options Neurol*. **17**, 344 (2015).
7. Krajmalnik-Brown, R., Lozupone, C., Kang, D. W. & Adams, J. B. Gut bacteria in children with autism spectrum disorders: challenges and promise of studying how a complex community influences a complex disease. *Microb. Ecol. Health Dis*. **26**, 26914 (2015).
8. Zheng, P. et al. Gut microbiome remodeling induces depressive-like behaviors through a pathway mediated by the host's metabolism. *Mol. Psychiatry* **21**, 786–796 (2016).
9. Möhle, L. et al. Ly6C$^{\mathrm{hi}}$ monocytes provide a link between antibiotic-induced changes in gut microbiota and adult hippocampal neurogenesis. *Cell Rep*. **15**, 1945–1956 (2016).
10. Hoban, A. E. et al. Regulation of prefrontal cortex myelination by the microbiota. *Transl. Psychiatry* **6**, e774 (2016).
11. Braniste, V. et al. The gut microbiota influences blood-brain barrier permeability in mice. *Sci. Transl. Med*. **6**, 263ra158 (2014).
12. Erny, D. et al. Host microbiota constantly control maturation and function of microglia in the CNS. *Nat. Neurosci*. **18**, 965–977 (2015).
13. Hoban, A. E. et al. The microbiome regulates amygdala-dependent fear recall. *Mol. Psychiatry* **23**, 1134–1144 (2018).
14. Lu, J. et al. Microbiota influence the development of the brain and behaviors in C57BL/6J mice. *PLoS ONE* **13**, e0201829 (2018).
15. Arentsen, T., Raith, H., Qian, Y., Forssberg, H. & Diaz Heijtz, R. Host microbiota modulates development of social preference in mice. *Microb. Ecol. Health Dis*. **26**, 29719 (2015).
16. Desbonnet, L., Clarke, G., Shanahan, F., Dinan, T. G. & Cryan, J. F. Microbiota is essential for social development in the mouse. *Mol. Psychiatry* **19**, 146–148 (2014).
17. Hepworth, M. R. et al. Group 3 innate lymphoid cells mediate intestinal selection of commensal bacteria-specific CD4$^+$ T cells. *Science* **348**, 1031–1035 (2015).
18. Pattwell, S. S. et al. Altered fear learning across development in both mouse and human. *Proc. Natl Acad. Sci. USA* **109**, 16318–16323 (2012).
19. Soliman, F. et al. A genetic variant BDNF polymorphism alters extinction learning in both mouse and human. *Science* **327**, 863–866 (2010).
20. Bravo, J. A. et al. Ingestion of *Lactobacillus* strain regulates emotional behavior and central GABA receptor expression in a mouse via the vagus nerve. *Proc. Natl Acad. Sci. USA* **108**, 16050–16055 (2011).
21. Sgritta, M. et al. Mechanisms underlying microbial-mediated changes in social behavior in mouse models of autism spectrum disorder. *Neuron* **101**, 246–259.e246 (2019).
22. Kipnis, J., Cohen, H., Cardon, M., Ziv, Y. & Schwartz, M. T cell deficiency leads to cognitive dysfunction: implications for therapeutic vaccination for schizophrenia and other psychiatric conditions. *Proc. Natl Acad. Sci. USA* **101**, 8180–8185 (2004).
23. Miyajima, M. et al. Metabolic shift induced by systemic activation of T cells in PD-1-deficient mice perturbs brain monoamines and emotional behavior. *Nat. Immunol*. **18**, 1342–1352 (2017).
24. Filiano, A. J. et al. Unexpected role of interferon-γ in regulating neuronal connectivity and social behaviour. *Nature* **535**, 425–429 (2016).
25. Tovote, P., Fadok, J. P. & Lüthi, A. Neuronal circuits for fear and anxiety. *Nat. Rev. Neurosci*. **16**, 317–331 (2015).
26. Dragunow, M. & Faull, R. The use of *c-fos* as a metabolic marker in neuronal pathway tracing. *J. Neurosci. Methods* **29**, 261–265 (1989).
27. Gale, G. D. et al. Role of the basolateral amygdala in the storage of fear memories across the adult lifetime of rats. *J. Neurosci*. **24**, 3810–3815 (2004).
28. Thion, M. S. et al. Microbiome influences prenatal and adult microglia in a sex-specific manner. *Cell* **172**, 500–516.e516 (2018).
29. Kierdorf, K. et al. Microglia emerge from erythromyeloid precursors via Pu.1- and Irf8-dependent pathways. *Nat. Neurosci*. **16**, 273–280 (2013).
30. Yuste, R. & Bonhoeffer, T. Morphological changes in dendritic spines associated with long-term synaptic plasticity. *Annu. Rev. Neurosci*. **24**, 1071–1089 (2001).
31. Yuste, R. & Denk, W. Dendritic spines as basic functional units of neuronal integration. *Nature* **375**, 682–684 (1995).
32. Trachtenberg, J. T. et al. Long-term *in vivo* imaging of experience-dependent synaptic plasticity in adult cortex. *Nature* **420**, 788–794 (2002).
33. Matsuzaki, M., Honkura, N., Ellis-Davies, G. C. & Kasai, H. Structural basis of long-term potentiation in single dendritic spines. *Nature* **429**, 761–766 (2004).
34. Lai, C. S., Franke, T. F. & Gan, W. B. Opposite effects of fear conditioning and extinction on dendritic spine remodelling. *Nature* **483**, 87–91 (2012).
35. Sudo, N. et al. Postnatal microbial colonization programs the hypothalamic-pituitary-adrenal system for stress response in mice. *J. Physiol. (Lond.)* **558**, 263–275 (2004).
36. Ivanov, I. I. et al. Induction of intestinal Th17 cells by segmented filamentous bacteria. *Cell* **139**, 485–498 (2009).
37. Atarashi, K. et al. Induction of colonic regulatory T cells by indigenous *Clostridium* species. *Science* **331**, 337–341 (2011).
38. Garrett, W. S. et al. Enterobacteriaceae act in concert with the gut microbiota to induce spontaneous and maternally transmitted colitis. *Cell Host Microbe* **8**, 292–300 (2010).
39. Schaedler, R. W. & Dubos, R. J. The fecal flora of various strains of mice. Its bearing on their susceptibility to endotoxin. *J. Exp. Med*. **115**, 1149–1160 (1962).
40. Tautenhahn, R., Patti, G. J., Rinehart, D. & Siuzdak, G. XCMS Online: a web-based platform to process untargeted metabolomic data. *Anal. Chem*. **84**, 5035–5039 (2012).
41. Shaw, W. Increased urinary excretion of a 3-(3-hydroxyphenyl)-3-hydroxypropionic acid (HPHPA), an abnormal phenylalanine metabolite of *Clostridia* spp. in the gastrointestinal tract, in urine samples from patients with autism and schizophrenia. *Nutr. Neurosci*. **13**, 135–143 (2010).
42. Keşli, R., Gökçen, C., Buluğ, U. & Terzi, Y. Investigation of the relation between anaerobic bacteria genus *Clostridium* and late-onset autism etiology in children. *J. Immunoassay Immunochem*. **35**, 101–109 (2014).
43. Yeh, Y. C. et al. Indoxyl sulfate, not p-cresyl sulfate, is associated with cognitive impairment in early-stage chronic kidney disease. *Neurotoxicology* **53**, 148–152 (2016).
44. Hsiao, E. Y. et al. Microbiota modulate behavioral and physiological abnormalities associated with neurodevelopmental disorders. *Cell* **155**, 1451–1463 (2013).

---

[1]Jill Roberts Institute for Research in Inflammatory Bowel Disease, Weill Cornell Medicine, Cornell University, New York, NY, USA. [2]Feil Family Brain and Mind Research Institute, Weill Cornell Medicine, Cornell University, New York, NY, USA. [3]Department of Psychiatry, Weill Cornell Medicine, Cornell University, New York, NY, USA. [4]Sackler Institute for Developmental Psychobiology, Weill Cornell Medicine, Cornell University, New York, NY, USA. [5]Department of Pharmacology, Weill Cornell Medicine, Cornell University, New York, NY, USA. [6]Boyce Thompson Institute and Department of Chemistry and Chemical Biology, Cornell University, Ithaca, NY, USA. [7]Klarman Cell Observatory, Broad Institute of MIT and Harvard, Cambridge, MA, USA. [8]Center for Biomedical Science and Bioelectronic Medicine, Feinstein Institute for Medical Research, Northwell Health, Manhasset, NY, USA. [9]Elmezzi Graduate School, Feinstein Institute for Medical Research, Northwell Health, Manhasset, NY, USA. [10]Department of Surgery, Northshore University Hospital, Northwell Health, Manhasset, NY, USA. [11]Donald and Barbara Zucker School of Medicine at Hofstra/Northwell, Hempstead, NY, USA. [12]Howard Hughes Medical Institute, Koch Institute of Integrative Cancer Research, Department of Biology, Massachusetts Institute of Technology, Cambridge, MA, USA. [13]Friedman Center for Nutrition and Inflammation, Joan and Sanford I. Weill Department of Medicine, Department of Microbiology and Immunology, Weill Cornell Medicine, Cornell University, New York, NY, USA. *e-mail: col2004@med.cornell.edu; dartis@med.cornell.edu

Methods

No statistical methods were used to predetermine sample size. The experiments were not randomized and investigators were not blinded to allocation during experiments and outcome assessment, except for dendritic spine imaging data analysis, in which the raters were blinded to experimental conditions.

Mice

C57BL/6J (Jax 664), *Rag1*$^{-/-}$ (Jax 2216), Thy1-YFP-H (Jax 3782) and BALB/c (Jax 651) mice were purchased from The Jackson Laboratory and bred in-house. Male mice were used at 7–16 weeks of age. In individual experiments, all mice were age-matched. All mice were maintained under SPF conditions on a 12-h light–dark cycle, and provided food and water ad libitum. Germ-free C57BL/6J mice and gnotobiotic mice were maintained at Weill Cornell Medical College, New York. All mouse experiments were approved by, and performed in accordance with, the Institutional Animal Care and Use Committee guidelines at Weill Cornell Medicine.

Antibiotic treatment

Mice were provided autoclaved drinking water supplemented with a cocktail of broad-spectrum antibiotics as previously described[17]: ampicillin (0.5 mg/ml, Santa Cruz), gentamicin (0.5 mg/ml, Gemini Bio-Products), metronidazole (0.5 mg/ml Sigma), neomycin (0.5 mg/ml, Sigma), vancomycin (0.25 mg/ml, Chem-Impex International), and saccharin (4 mg/ml, Sweet'N Low, Cumberland Packing). Sweet'N Low was added to make the antibiotic cocktail more palatable. Antibiotic treatment was started two weeks before the experiments and continued for the duration of the experiments. Following antibiotic treatment mice exhibited no significant differences in weight gain, food or water intake (measured by Promethion metabolic cages) or perception of pain[45].

Fear conditioning and extinction assays

Fear conditioning and extinction assays were performed as previously described[18,19]. For fear conditioning, mice were placed in shock chambers (Coulbourn Instruments), which were scented with 0.1% peppermint in 70% EtOH. After 2 min of habituation, mice were fear conditioned with 3 tone–shock pairings consisting of a 30-s (5 kHz, 70 dB) tone (conditioned stimulus, CS) that co-terminated with a 1-s (0.7 mA) foot shock (unconditioned stimulus, US). Intertrial intervals (ITIs) between each tone–shock pairing were 30 s. After the final tone–shock pairing, mice remained in the conditioning chambers for 1 min before being returned to their home cages.

For the classical 3-day (that is, 3-session) fear extinction, 24 h after fear conditioning, mice were placed in extinction chambers (different shape from the conditioning chambers), which were scented with 0.1% lemon in 70% EtOH. After 2 min of habituation, mice were exposed to 5 presentations of the tone (CS) in the absence of the shock (US). Each tone lasted for 30 s with an ITI of 30 s. After the final tone presentation, mice remained in the extinction chambers for 1 min before being returned to their home cages. Fear extinction sessions were repeated daily for three days.

For single-session 30-tone fear extinction, 20 min after fear conditioning, mice were placed in extinction chambers. After 2 min of habituation, mice were exposed to 30 presentations of the tone (CS) in the absence of the shock (US). Each tone lasted for 30 s with an ITI of 30 s. Extinction trials were binned into early and late sessions, with the early session representing the average of trials 1–15, and late trials representing the average of trials 16–30.

Experiments were controlled by Graphic State software (Coulbourn instruments). Mice were video-recorded for subsequent analysis.

Fear behaviour

Mouse freezing behaviour was scored automatically using previously validated MATLAB code for automated phenotyping of mouse behaviour[46]. Per cent time spent freezing (freezing (%)) was calculated by dividing the amount of time spent freezing during the 30-s tone presentations by the duration of the tone.

Immunofluorescence staining

Brain sections were prepared and stained for c-FOS, synaptophysin or PSD-95 expression as previously described[47]. All steps were carried out at room temperature unless otherwise specified. Ninety minutes after fear extinction session 3, mice were anaesthetized by intraperitoneal injection of Euthasol and perfused with PBS followed by 4% paraformaldehyde. Brains were collected, fixed in 4% paraformaldehyde overnight, and dehydrated in 30% sucrose at 4 °C. Coronal sections (40 µm) were cut using a sliding microtome frozen by powdered dry ice. Six sets of serial sections were collected in Eppendorf tubes each containing 2 ml cryoprotectant (30% glycerol and 30% ethylene glycol in 0.1 M sodium phosphate, pH 7.4) and stored at −20 °C. Free-floating serial sections (1 in every 3) were washed in TBS, incubated for 30 min in blocking buffer (4% normal horse serum, 1% BSA and 0.2% Triton X-100 in TBS) and incubated overnight at 4 °C with rabbit anti-c-FOS primary antibody (sc-52, Santa Cruz), or mouse anti-synaptophysin (SAB4200544, Sigma-Aldrich) or PSD-95 (7E3-1B8, Sigma-Aldrich) diluted 1:1,000 in the blocking buffer. Sections were then washed in TBS and incubated for 2 h with Alexa-Fluor-555-labelled donkey anti-rabbit or anti-mouse antibody (Invitrogen) diluted 1:500 in TBS with 0.2% Triton X-100. Sections were again washed, mounted on chromalum/gelatin-coated slides and air-dried for 2 h in darkness. Slides were coverslipped with water-soluble glycerol-based mounting medium containing DAPI and sealed with nail polish.

Estimation of cell densities of c-FOS$^+$ neurons in BLA and IL was performed with StereoInvestigator 9.0 (MicroBrightField). In brief, serial sections (every third section, 120 µm) were numbered by rostra-caudal order, and contours of BLA and IL were traced by referring to the Allen Brain Atlas (Allen Institute). All cells across all sections per mouse were counted. Individual cell density was calculated for each mouse by dividing the total sampled cell numbers by the total volume of the region.

For synaptophysin and PSD-95 images, confocal microscopy was performed with a Zeiss LSM 880 Laser Scanning Confocal Microscope using 63× oil immersion lens. Images were acquired with 2× digital zoom. Image stacks were 5 µm in thickness with *z*-step size of 0.5 µm, and were analysed using ImageJ software (http://rsbweb.nih.gov/ij/).

Intracranial window implantation

Mice were anaesthetized with isoflurane (induction, 5%; maintenance, 1–2%) and administered dexamethasone (1 mg/kg, i.p.) to reduce brain swelling and metacam (2 mg/kg, i.p.) as a prophylactic analgesic. Scalp fur was trimmed, and the skull surface was exposed with a midline scalp incision. Bupivicaine (0.05 ml, 5 mg/ml) was administered topically as a second prophylactic analgesic. A circular titanium head plate was positioned over the region to be imaged (1.7 mm anterior to the bregma suture and centred over the midline) using dental cement (Metabond). A high-speed dental drill (Model EXL-M40, Osada) and 0.5-mm burr were used to open a small (about 4-mm) craniotomy. A 3-mm round coverslip (Warner Instruments) was lowered through the craniotomy to rest on top of the brain using a digital micromanipulator. The window was then fixed to the skull using veterinary adhesives (first Vetbond, then Metabond).

Viral injection

AAV5–hSyn–GCaMP6s was obtained from the UPenn Vector Core. Viral injection surgeries were performed with mice (8–10 weeks of age) under isoflurane anaesthesia (induction, 5%; maintenance, 1–2%) with regular monitoring for stable respiratory rate and absent tail pinch response. The scalp was shaved, and mice were fixed in a stereotactic frame (Kopf Instruments) with non-rupturing ear bars. A heating pad was used to prevent hypothermia. A midline incision was made to expose the skull and bupivacaine was applied onto the skull for local anaesthesia. Virus injections (1,000 nl) were delivered with a 10-µl Hamilton syringe and

33-gauge bevelled needle, injected at 100 nl/min using an injection pump (World Precision Instruments). Injection coordinates relative to Bregma were: 1.7 mm anterior, 0.4 mm lateral, and 1.3 mm ventral. Following injection, the injection needle was held at the injection site for 2 min then slowly withdrawn. The skin was then closed using Vetbond (3M) and the mice recovered on a heating pad before being returned to their home cages.

Transcranial two-photon imaging

Dendritic spine imaging was conducted as previously described[48]. In brief, image stacks of dendritic segments were acquired using a two-photon laser scanning microscope (Olympus RS) equipped with a scanning galvanometer and a Spectra-Physics Mai Tai DeepSee laser tuned to 920 nm, and a 25×, long working distance water-immersion microscope objective (NA = 1.05, Olympus). Fluorescence was detected through gallium arsenide phosphide photomultiplier tubes using the Fluoview acquisition software (Olympus), and images were collected in the green channel using an F30FGR bandpass filter (Semrock). All imaging experiments began by obtaining a low-magnification *z*-stack (no digital zoom) to aid in relocating the same sites repeatedly over time, in conjunction with vascular landmarks and the contours of the prism. For spine imaging experiments, we acquired *z*-stacks (512 × 512 pixels, 2-μs pixel dwell time, 0.75–1-μm step size) with 3× digital zoom through up to 250 μm of tissue in *z*. Spine imaging experiments occurred under KX anaesthesia (ketamine 100 mg/ml and xylazine 10 mg/ml, at dosages of 0.1 ml/10 g body weight). For calcium imaging experiments, we acquired time-lapse images (512 × 512 pixels, 3 frames per second, about 1,450 frames,) spanning an area of the mPFC measuring approximately 508 μm by 508 μm. All calcium imaging experiments were carried out on awake mice. For repeated imaging over intervals of days, the procedure above was repeated, and the region to be imaged was identified by referring to vascular landmarks and the contours of the cranial window.

Spine imaging analysis

Spine remodelling dynamics were quantified as previously described[48]. Image stacks were analysed using ImageJ software (http://rsbweb.nih.gov/ij/). Raters blinded to experimental condition compared pairs of images of the same dendritic segment and identified stable spines (present in image 1 and 2), eliminated spines (present in image 1 but not in image 2) and formed spines (present in image 2 but not in image 1), each quantified as a percentage of the total number of spines identified in the initial image. Filopodia were defined as dendritic protrusions with a length exceeding three times their maximum width and were excluded from spine remodelling analyses.

Calcium imaging analysis

Preprocessing. We used standard, validated procedures for preprocessing and analysing calcium imaging time series data. *X*–*Y* motion artefacts were corrected using the ImageJ plugin 'Image Stabilizer' created by K. Li and S. Kang (https://www.cs.cmu.edu/~kangli/code/Image_Stabilizer.html). Image time series were segmented into individual cells using custom MATLAB scripts based on an established sorting algorithm that combines independent components analysis and image segmentation based on threshold intensity, variance, and skewness in the *X*–*Y* motion-corrected dataset[49–51]. Image segmentation results were manually inspected for quality control. Fluorescence signal time series ($\Delta F/F$: change in fluorescence divided by baseline fluorescence) were calculated for each individual neuronal segment: a 40-s sliding window was used to calculate the baseline fluorescence for each cell, accounting for both differences in GCaMP expression and de-trending for slow timescale changes in fluorescence[50].

Analysis. First, we tested for cells exhibiting tone-sensitive activity, using repeated-measures ANOVA to identify cells with a statistically significant increase (Fig. 4f) or decrease (Fig. 4d) in activity during tone presentations, compared to their activity during a two-minute pre-tone baseline period. To estimate statistical significance while accounting for autocorrelation in calcium transient time series and correcting for multiple comparisons, we repeated this analysis 10,000 times for each cell after shuffling the timing of the baseline period and the timing of the tone onsets and selected a *P* value threshold to limit the FDR to less than 5%. Next, to test for group (ABX versus control) effects on activity in each of these cell populations (Fig. 4e, g), we used a two-factor (time and group) repeated-measures ANOVA and post-hoc linear contrasts to test for between-group differences in activity during each task epoch (baseline, tone on and tone off). Finally, to test for cells that also encoded the precise timing of the tones, exhibiting tone-locked activity that increased or decreased in response to the onset of each tone, we used a procedure analogous to the one described above, using repeated-measures ANOVA to test for changes in activity in the tone on versus tone off epochs; estimating statistical significance in shuffled data as above; and testing for group effects on activity using a two-factor (time and group) repeated-measures ANOVA (Fig. 4h, i).

RNA-seq

Mouse mPFC was dissected by referring to the Allen Brain Atlas. Coordinates relative to bregma are: 1.3 to 2.8 mm anterior, −1 to 1 mm lateral, and 0 to 1 mm ventral. RNA was extracted using Trizol (Invitrogen) and chloroform and further purified using the RNAeasy mini spin columns (Qiagen). RNA-seq libraries were prepared and sequenced by the Epigenomics Core at Weill Cornell Medicine on an Illumina HiSeq 2500, producing 50-bp single-end reads. Sequenced reads were demultiplexed using CASAVA v1.8.2 and adapters trimmed using FLEXBAR v2.4[52].

RNA-seq analysis

Sequenced reads were aligned to the mouse genome GRCm38/mm10 using STAR v2.3.0[53]. Reads counts at the gene level were calculated using Rsubread[54]. Normalization for library size and differential expression analysis were performed using DESeq2[55] v1.18. Only genes with at least ten raw reads in each sample were tested for differential expression. PERMANOVA[56] was used to test whether antibiotic treatment accounted for a significant portion of the variance in gene expression after fear extinction. Specifically, expression of the 500 genes with the highest variance (after applying the variance stabilization transformation of DESeq2[55]) was analysed using the adonis function of the vegan R package (https://CRAN.R-project.org/package=vegan) using the Euclidean metric and 20,000 permutations. Differentially expressed genes were used for GO enrichment analysis (http://www.pantherdb.org/)[57], KEGG analysis (https://www.genome.jp/kegg)[58] and STRING analysis (https://string-db.org/)[59].

Brain-resident immune cell isolation and flow cytometry

Brain-resident immune cells were isolated using Percoll gradients[60]. Mice were anaesthetized and perfused with ice-cold HBSS. Brains were removed, homogenized, resuspended with 30% Percoll, and layered on top of 70% Percoll. After centrifugation (500*g*, 30 min), immune cells gathered in the 30–70% interphase.

For flow cytometric analyses, cells were washed, incubated with purified anti-mouse CD16/CD32 (clone 93, Biolegend) to block the Fc receptors, and then stained with anti-CD45 (clone 30-F11, Biolegend), anti-CD4 (clone RM4-5, eBioscience), anti-CD8a (clone 53-6.7, BD Biosciences), anti-CD19 (clone 1D3, eBioscience), anti-CD11b (clone M1/70, eBioscience), anti-CD11c (clone N418, eBioscience), anti-F4/80 (clone BM8, eBioscience), anti-LY6G (clone 1A8-Ly6g, eBioscience), anti-LY6C (clone HK1.4, eBioscience) and anti-CSF1R (clone AFS98, eBioscience). Data were collected on a LSRFortessa cytometer (BD Biosciences) and analysed with FlowJo software (Tree Star). Dead cells were excluded from analyses based on LIVE/DEAD Fixable Aqua dead cell staining (Invitrogen). Non-singlet events were excluded from analyses based on the side scatter height (SSC-H) versus side scatter width (SSC-W), and then the forward scatter height (FSC-H) versus forward scatter width (FSC-W) characteristics.

Microbial colonization

For ex-GF mice colonized when they were adults (ex-GF_adult), dirty bedding from SPF mice was placed in the GF cages of 8-week-old GF mice two weeks before the fear conditioning and extinction assay. For ex-GF mice colonized when they were weaned (ex-GF_weaning), 3-week-old GF mice were co-housed with 3-week-old SPF mice until they were 8 weeks old and then subjected to the fear conditioning and extinction assay.

Fostering of pups

C57BL/6J GF and control SPF newborn pups were fostered by BALB/c mothers until weaning.

16S qPCR

DNA was isolated from faecal samples of control and ABX mice using the DNeasy PowerSoil kit (Qiagen). Equal amounts of purified faecal DNA (4 ng per reaction) were added to qPCR reactions with universal 16S primers using SYBR green chemistry (UniF340: 5′-ACTCCTACGGGAGGCAGCAGT-3′; UniR514: 5′-ATTACCGCGGCTGCTGGC-3′). 16S DNA levels in each sample were normalized to the average of the control mouse group.

16S amplicon sequencing and analysis

16S rRNA gene sequencing methods were adapted from the methods developed for the NIH-Human Microbiome Project (https://hmpdacc.org/). In brief, bacterial genomic DNA was extracted using MO BIO PowerSoil DNA Isolation Kit (MO BIO Laboratories). The 16S rDNA V4 region was amplified by PCR and sequenced in the MiSeq platform (Illumina) using the 2 × 250-bp paired-end protocol. Raw reads were processed and clustered into operational taxonomic units (OTUs) using USEARCH version 11[61]. Specifically, reads were demultiplexed and read pairs merged, with a maximum of five mismatching bases in the overlap region, as well as a minimum sequence agreement of 80%. PhiX contaminant sequences were removed, and merged sequences were filtered according to FASTQ quality scores using a maximum expected error number of 0.1. Filtered sequences were clustered into OTUs at a 97% identity threshold using the USEARCH cluster_otus command with default settings. Merged reads (unfiltered) were mapped to the OTU representative sequences, generating an OTU table. Taxonomic classification of OTU representative sequences was performed with the USEARCH SINTAX command with a confidence score of 0.8, using version 16 of the RDP 16S training set[62]. Diversity estimation and principal coordinates analysis (PCoA) ordination were performed using the phyloseq R package[63] after subsampling the OTU table to even depth.

snRNA-seq

Nuclei were extracted from four frozen mPFC samples (two from ABX mice and two from control mice) with a glass dounce tissue grinder set (Millipore Sigma no. D8938) and Nuclei EZ Prep (Millipore Sigma no. NUC101-1kt). Each sample was dounced with pestles A and B (24× each) in 2 ml EZ prep buffer, washed with 5 ml EZ prep, and resuspended in 1 ml resuspension buffer (1× PBS, 0.1% BSA, 25 U/ml recombinant RNase inhibitor, Takara 2313B). Single nucleus suspensions were strained through a 35-µm cell strainer (Corning 352235), visually inspected under a microscope, and loaded onto 3′ library chips as per the manufacturer's protocol for the Chromium Single Cell 3′ Library & Gel Bead kit (v.3) (10X Genomics 1000092). For each sample, an input of 11,000 nuclei was added to each channel. Libraries were sequenced at a mean depth of 21,714 reads per nucleus on a HiSeqX.

snRNA-seq data processing

Demultiplexed FASTQ files were generated using Cell Ranger v2.0. Reads were aligned to the mm10 mouse transcriptome containing pre-mRNA annotations, similarly to previously described[64], to generate raw gene expression matrices (nuclei by genes). Expression matrices across all four samples were merged and loaded into Scanpy (version 1.4.0)[65]. Genes found in fewer than three nuclei were filtered out. Nuclei were filtered out using the following criteria: fewer than 600 genes (likely to be empty droplets), more than 5,000 genes (likely to be doublets), >2% of reads mapping to mitochondrial genes, >0.1% of reads mapping to caspase genes to remove apoptotic cells. The resulting filtered matrix consisted of 38,649 nuclei and 22,451 genes. The filtered gene expression matrix was normalized within each nucleus, resulting in a filtered, nuclei-normalized matrix X, then log-normalized by calculating $\ln(X+1)$. Before selecting variable genes, we masked genes that contain highly repetitive regions in intronic regions that result in inflated read counts (PISD, Mylip, Gm17660) and highly expressed lncRNAs that affect within-nuclei normalization (Gm28928, Malat1). We selected 1,535 highly variable genes using the highly_variable_genes module in scanpy (min_mean = 0.1, max_mean = 3, min_disp = 0.8) for clustering analysis.

snRNA-seq data clustering

We first regressed out the number of UMIs and the number of genes. Each gene was then scaled to unit variance. We then conducted dimensionality reduction via PCA using the ARPACK SVD solver in scanpy, computed the k-nearest neighbour graph with PCs 1–40 and $k = 30$ nearest neighbours. Clusters were determined with unsupervised clustering using the Louvain algorithm[66,67] and resulted in 24 clusters. Differential expression analysis was conducted to find the top 100 genes enriched in each cluster with the rank_genes_groups module in scanpy using logistic regression[68]. We annotated clusters post hoc on the basis of known marker genes[69,70] among the top 100 enriched genes. For visualization, we embedded the profiles with UMAP (uniform manifold approximation and projection[71]).

Cell-type-specific differential expression analysis

To find DEGs between ABX and control mice for each cluster, we used statsmodels in Python to implement a mixed linear model for each cluster c. Specifically, we used the regression $Y_{i,c} \sim T + N + (1|B)$, in which $Y_{i,c}$ is the $\ln(X+1)$ expression vector for gene i across all nuclei in cluster c, T is a binary variable reflecting membership of the nucleus in either ABX or control sample, N is the number of genes detected in each nucleus, and B is a categorical variable denoting the 10× channel used for each sample to control for batch effects. We used a Bonferroni-corrected P value of 10^{-7} as the cut-off for significance. For plotting, we used DEGs that had a minimum $\log_2$(fold change) of 0.31 (absolute fold change of 1.24) in either direction, and independently found to be significant in at least two clusters. To rank clusters based on the number of DEGs (Extended Data Fig. 5b), we first randomly sampled 500 nuclei with replacement from each cluster to maintain comparable statistical power across clusters and re-ran the mixed linear model as described; all other plots and analyses, including GO enrichment, were based on the full list of DEGs obtained without downsampling.

Vagotomy

The following subdiaphragmatic vagotomies and pyloromyotomy procedure were modified from previously described procedures[72]. Mice were anaesthetized via IP injection of a ketamine (144 mg/kg)/xylazine (13 mg/kg) cocktail. A midline incision was made and the stomach was retracted inferiorly to expose the distal oesophagus and the gastroesophageal junction. The anterior (left) and posterior (right) branches of the vagus nerve were identified running alongside the oesophagus and severed distal to the hepatic branches. The stomach was then placed back into the anatomical position and a pyloromyotomy was performed using a bent 23-gauge needle. The superficial muscular layers were incised in a longitudinal fashion and closed transversely with 4-0 vicryl sutures. The peritoneum was then closed with a running 4-0 vicryl suture and the skin approximated with staples. Mice were allowed to recover from anaesthesia under a heat lamp and returned to the colony room once awake and ambulating. For non-vagotomized mice, the vagus nerve was gently exposed without further manipulation. Mice were monitored for seven days. The completeness of subdiaphragmatic vagotomy was verified by examining fluorescent label of the dorsal motor vagal nucleus (DMV) on brainstem sections one week after intraperitoneal injection of FluoroGold. The absence of fluorescent label in DMV neurons was accepted as a marker of complete vagotomy.

Mass spectrometry

High-resolution LC–MS analysis was performed on a Dionex 3000 UPLC coupled with a Thermo Q-exactive high-resolution mass spectrometer equipped with a HESI ion source. Metabolites were separated using a water–acetonitrile gradient on a Agilent Zorbax Eclipse XDB-C18 column (150 mm × 2.1 mm, particle size 1.8 μm) maintained at 40 °C; solvent A: 0.1% formic acid in water; solvent B: 0.1% formic acid in acetonitrile. The A–B gradient started at 1% B for 1 min after injection and increased linearly to 100% B at 15 min, using a flow rate of 0.5 ml/min. Mass spectrometer parameters: spray voltage 2.9 kV, capillary temperature 320 °C, prober heater temperature 300 °C; sheath, auxiliary, and spare gas 70, 2, and 0 ml/min, respectively; S-lens RF level 55, resolution 140,000 at m/z 200, AGC target 1×10^6. The instrument was calibrated weekly with positive and negative ion calibration solutions (Thermo-Fisher). Each sample was analysed in negative and positive modes using a m/z range of 100 to 1,500.

Feature detection, characterization and compound synthesis

LC–MS RAW files from triplicate faecal, serum and CSF samples from adult ex-GF_fostered, Ctrl_fostered and GF mice were converted to mzXML (profile mode) using MSConvert (ProteoWizard), followed by analysis using a customized XCMS R-script based on the centWave XCMS algorithm to extract features[40]. Resulting tables of all detected features were used to compute ex-GF_fostered mice versus GF mice and Ctrl_fostered mice versus GF mice peak area ratios. To select differential features, we applied a filter that retained entries with peak area ratios larger than 2 (down in GF mice) or smaller than 0.5 (up in GF mice). We manually curated the resulting list to remove false positive entries—that is, features that upon manual inspection of raw data were not differential. For the features that were verified to be differential, we examined elution profiles, isotope patterns, and MS1 spectra to find molecular ions and remove adducts, fragments, and isotope peaks.

The structures of the four differential compounds were confirmed by coinjection with synthesized or commercial samples. Phenyl sulfate and indoxyl sulfate were purchased from TCI America and Sigma-Aldrich, respectively. Pyrocatechol sulfate and 3-(3-sulfooxyphenyl)propanoic acid were prepared following a previously published procedure[73]. To a stirred solution of catechol (Sigma-Aldrich, 0.55 g, 5 mmol) or 3-(4-hydroxyphenyl)propionic acid (Sigma-Aldrich, 0.88 g 5 mmol) in dry pyridine (2.5 ml), sulfur trioxide pyridine complex (0.88 g, 6 mmol) was added at room temperature. The resulting mixtures were heated in an oil bath at 45 °C and stirred for 2 h. The reactions were then allowed to cool to ambient temperature and transferred separately to flasks each containing 25 ml of 1 N KOH cooled in an ice bath. To each of the aqueous mixtures was added 100 ml of 2-propanol and the two reactions were left at 4 °C for 16 h. At this point, the products were filtered off as white precipitates. The crude products were taken up in 50 ml (3:1 ethanol:water) and heated to reflux, hot filtered, and placed in the fridge for recrystallization. This last step was then repeated. Totals of 210 and 270 mg of pyrocatechol sulfate and 3-(3-sulfooxyphenyl)propanoic acid were obtained, corresponding to yields of about 20%.

Statistical analysis

Statistical tests were performed with Prism (GraphPad). Unless specifically indicated otherwise, Student's *t*-tests were used to compare endpoint means of different groups. Error bars depict the s.e.m.

Reporting summary

Further information on research design is available in the Nature Research Reporting Summary linked to this paper.

Code availability

The algorithm used for automated scoring of freezing behaviour is available at https://www.seas.upenn.edu/~molneuro/software.html. The algorithm used for motion artefact correction in 2P calcium imaging data is available at http://www.cs.cmu.edu/~kangli/code/Image_Stabilizer.html. All other analysis code is available from the corresponding author upon reasonable request.

Data availability

RNA-seq data, 16S rRNA-seq data and snRNA-seq data are available at Gene Expression Omnibus and BioProject under accession numbers GSE134808, PRJNA556230 and GSE135326, respectively. All datasets generated and/or analysed during the current study are presented in this published article, the accompanying Source Data or Supplementary Information, or are available from the corresponding author upon reasonable request.

45. Kang, M. et al. The effect of gut microbiome on tolerance to morphine mediated antinociception in mice. *Sci. Rep.* **7**, 42658 (2017).
46. Patel, T. P. et al. An open-source toolbox for automated phenotyping of mice in behavioral tasks. *Front. Behav. Neurosci.* **8**, 349 (2014).
47. Dincheva, I. et al. FAAH genetic variation enhances fronto-amygdala function in mouse and human. *Nat. Commun.* **6**, 6395 (2015).
48. Liston, C. et al. Circadian glucocorticoid oscillations promote learning-dependent synapse formation and maintenance. *Nat. Neurosci.* **16**, 698–705 (2013).
49. Mukamel, E. A., Nimmerjahn, A. & Schnitzer, M. J. Automated analysis of cellular signals from large-scale calcium imaging data. *Neuron* **63**, 747–760 (2009).
50. Dombeck, D. A., Khabbaz, A. N., Collman, F., Adelman, T. L. & Tank, D. W. Imaging large-scale neural activity with cellular resolution in awake, mobile mice. *Neuron* **56**, 43–57 (2007).
51. Rajasethupathy, P. et al. Projections from neocortex mediate top-down control of memory retrieval. *Nature* **526**, 653–659 (2015).
52. Dodt, M., Roehr, J. T., Ahmed, R. & Dieterich, C. FLEXBAR—flexible barcode and adapter processing for next-generation sequencing platforms. *Biology (Basel)* **1**, 895–905 (2012).
53. Dobin, A. et al. STAR: ultrafast universal RNA-seq aligner. *Bioinformatics* **29**, 15–21 (2013).
54. Liao, Y., Smyth, G. K. & Shi, W. The Subread aligner: fast, accurate and scalable read mapping by seed-and-vote. *Nucleic Acids Res.* **41**, e108 (2013).
55. Love, M. I., Huber, W. & Anders, S. Moderated estimation of fold change and dispersion for RNA-seq data with DESeq2. *Genome Biol.* **15**, 550 (2014).
56. Anderson, M. J. A new method for non-parametric multivariate analysis of variance. *Austral Ecol.* **26**, 32–46 (2001).
57. Mi, H., Muruganujan, A., Casagrande, J. T. & Thomas, P. D. Large-scale gene function analysis with the PANTHER classification system. *Nat. Protocols* **8**, 1551–1566 (2013).
58. Kanehisa, M. & Goto, S. KEGG: Kyoto encyclopedia of genes and genomes. *Nucleic Acids Res.* **28**, 27–30 (2000).
59. Snel, B., Lehmann, G., Bork, P. & Huynen, M. A. STRING: a web-server to retrieve and display the repeatedly occurring neighbourhood of a gene. *Nucleic Acids Res.* **28**, 3442–3444 (2000).
60. Pino, P. A. & Cardona, A. E. Isolation of brain and spinal cord mononuclear cells using percoll gradients. *J. Vis. Exp.* **48**, 2348 (2011).
61. Edgar, R. C. Search and clustering orders of magnitude faster than BLAST. *Bioinformatics* **26**, 2460–2461 (2010).
62. Cole, J. R. et al. Ribosomal Database Project: data and tools for high throughput rRNA analysis. *Nucleic Acids Res.* **42**, D633–D642 (2014).
63. McMurdie, P. J. & Holmes, S. phyloseq: an R package for reproducible interactive analysis and graphics of microbiome census data. *PLoS ONE* **8**, e61217 (2013).
64. Bakken, T. E. et al. Single-nucleus and single-cell transcriptomes compared in matched cortical cell types. *PLoS ONE* **13**, e0209648 (2018).
65. Wolf, F. A., Angerer, P. & Theis, F. J. SCANPY: large-scale single-cell gene expression data analysis. *Genome Biol.* **19**, 15 (2018).
66. Blondel, V. D., Guillaume, J.-L., Lambiotte, R. & Lefebvre, E. Fast unfolding of communities in large networks. *J. Stat. Mech.* **2008**, P10008 (2008).
67. Traag, V. A. Faster unfolding of communities: speeding up the Louvain algorithm. *Phys. Rev. E* **92**, 032801 (2015).
68. Ntranos, V., Yi, L., Melsted, P. & Pachter, L. A discriminative learning approach to differential expression analysis for single-cell RNA-seq. *Nat. Methods* **16**, 163–166 (2019).
69. Zhang, Y. et al. An RNA-sequencing transcriptome and splicing database of glia, neurons, and vascular cells of the cerebral cortex. *J. Neurosci.* **34**, 11929–11947 (2014).
70. Habib, N. et al. Massively parallel single-nucleus RNA-seq with DroNc-seq. *Nat. Methods* **14**, 955–958 (2017).

71. McInnes, L., Healy, J., Saul, N. & Großberger, L. UMAP: uniform manifold approximation and projection. *J. Open Source Softw*. **3**, 861 (2018).
72. Dezfuli, G. et al. Subdiaphragmatic vagotomy with pyloroplasty ameliorates the obesity caused by genetic deletion of the melanocortin 4 receptor in the mouse. *Front. Neurosci*. **12**, 104 (2018).
73. Edwards, D. R., Lohman, D. C. & Wolfenden, R. Catalytic proficiency: the extreme case of S-O cleaving sulfatases. *J. Am. Chem. Soc*. **134**, 525–531 (2012).

Acknowledgements We thank the members of the Artis and Liston laboratories for discussion and reading of the manuscript; G. Eraslan, S. Simmons, and C. Smillie for discussions about the snRNA-seq analyses; and the Metabolic Phenotyping Center of Weill Cornell Medicine for technical advice and support. The summary cartoon (Extended Data Fig. 10f) was created with BioRender.com. This work was supported by the Jill Roberts Institute (to G.G.P.), JSPS Overseas Research Fellowships (to S.M.), the National Institute of General Medical Sciences (1R35GM118182-01, to K.J.T.), the National Institute of Allergy and Infectious Diseases (1P01AI102852-01A1, to K.J.T. and S.S.C.), the National Institutes of Health (NS052819, to F.S.L), the Rita Allen Foundation, the One Mind Institute, the Klingenstein-Simons Foundations, the Brain and Behavior Research Foundation, and the National Institutes of Mental Health (R01 MH109685, R01 MH118451) (all to C.L.), the National Institutes of Health (AI074878, AI095466, AI095608 and AI102942), the Burroughs Wellcome Fund, the Crohn's and Colitis Foundation and the Rosanne H. Silbermann Foundation (all to D.A.). F.C.S. is a Faculty Scholar of the Howard Hughes Medical Institute. This work was supported by the Klarman Cell Observatory at the Broad Institute. A.R. is a Howard Hughes Medical Institute Investigator.

Author contributions C.C. carried out most of the experiments and analysed the data. M.H.M., D.J., T.H.W., H.C., A.M.K., T.T., M.E.A., L.Z., N.J.B., R.Y., S.M., C.N.P., A.L., H.C.M., F.T., S.S.C., K.J.T., A.R., F.C.S. and F.S.L. helped with experiments. H.C. and A.R. performed snRNA-seq and analysis. G.G.P. performed bulk RNA-seq and 16S rDNA-seq analysis. D.A., C.L. and C.C. conceived the project, analysed data, and wrote the manuscript with input from all co-authors.

Competing interests A.R. is an SAB member of ThermoFisher Scientific and Syros Pharmaceuticals and a co-founder and equity holder of Celsius Therapeutics. D.A. has contributed to scientific advisory boards at MedImmune, Pfizer, FARE, and the KRF. The other authors declare no competing interests.

Additional information

Supplementary information is available for this paper at https://doi.org/10.1038/s41586-019-1644-y.

Correspondence and requests for materials should be addressed to C.L. or D.A.

Peer review information *Nature* thanks Drew Kiraly and the other, anonymous, reviewer(s) for their contribution to the peer review of this work.

Reprints and permissions information is available at http://www.nature.com/reprints.

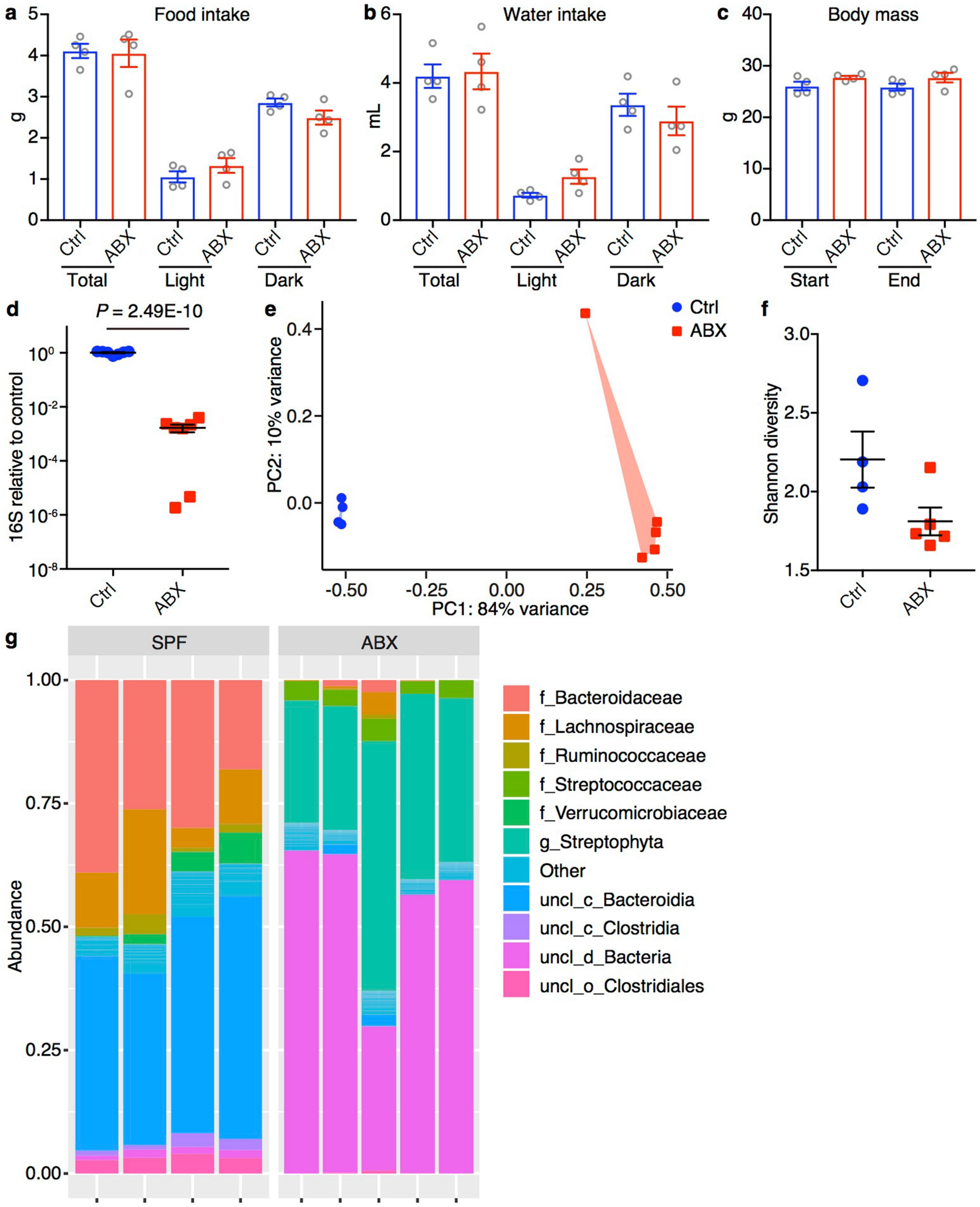

Extended Data Fig. 1 | Antibiotic treatment results in bacterial community restructuring. **a**–**c**, Food intake (**a**), water intake (**b**) and weight gain (**c**) of the mice measured using the Promethion Metabolic Cage System. Antibiotic treatment was started two weeks before the experiment and continued for the duration of the experiment. For food (**a**) and water intake (**b**), the mice were acclimated to the system for the first four days followed by one day of data collection. Body mass (**c**) of the mice was measured at the beginning (Start) and the end (End) of the 5-day experiment. *n* = 4 mice per group. Mean ± s.e.m. Total, full day. Light and Dark denote the light and dark periods of the 12-h cycle. **d**, 16S rDNA gene copies as quantified by real-time PCR with reverse transcription (RT–PCR) from stool pellets collected from control or ABX mice. Data pooled from two independent experiments. *n* = 7 mice per group. Mean ± s.e.m.; unpaired two-sided *t*-test. **e**–**g**, PCoA (**e**), alpha-diversity Shannon index (**f**) and taxonomic classification (**g**) of 16S rDNA in stool pellets collected from control or ABX mice. Control *n* = 4, ABX *n* = 5. For PCoA plot PERMANOVA: *F* = 33.579, Df = 1, *P* = 0.00804. For phylogenetic classification 'f_', 'g_', 'uncl_c_', 'uncl_d_' and 'uncl_o_' stand for 'family_', 'genus_', 'unclassified_class_', 'unclassified_domain_' and 'unclassified_order_', respectively. 'uncl_d_Bacteria' matches exactly to mitochondria or chloroplasts, probably from the food. Mean ± s.e.m. in **f**.

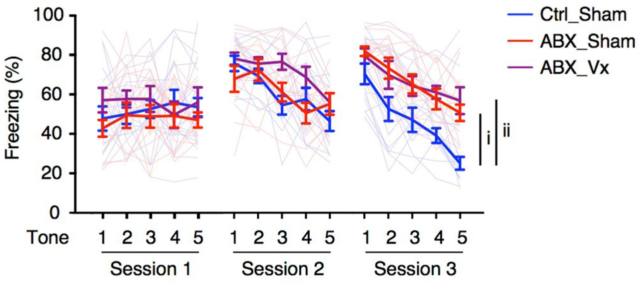

Extended Data Fig. 2 | Antibiotic-treated mice retain deficits in extinction learning after vagotomy. Fear extinction in sham-operated control (Ctrl_Sham) or ABX mice (ABX_Sham) and in vagotomised ABX mice (ABX_Vx) mice over the course of 3 days or sessions. Ctrl_Sham *n* = 10, ABX_Sham *n* = 10, ABX_Vx *n* = 12. Mean ± s.e.m.; AUC was calculated for each mouse within each group, followed by unpaired two-sided *t*-test between groups. *P* values are as follows: i, 2.57×10^{-7}; ii, 9.21×10^{-8}.

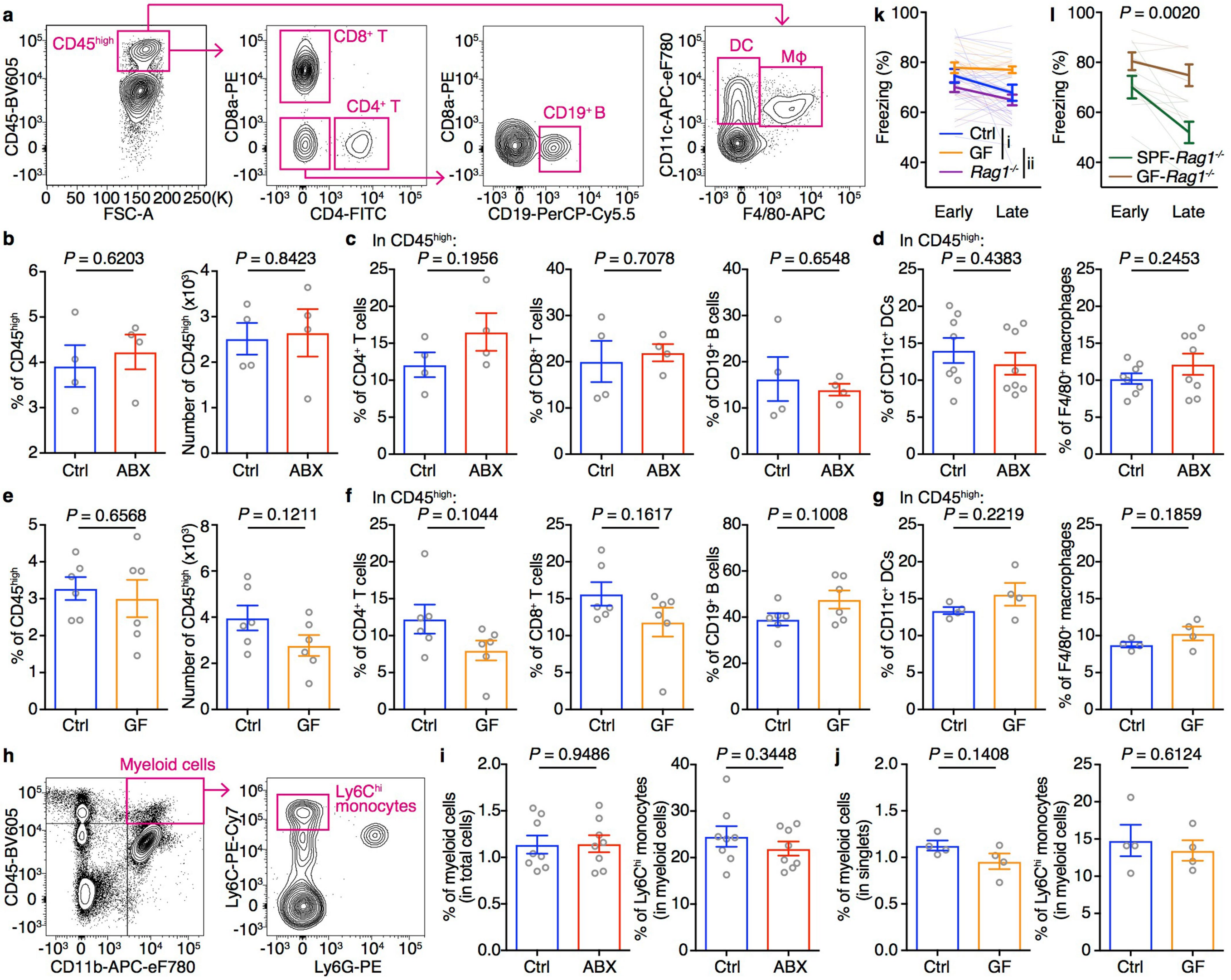

Extended Data Fig. 3 | Comparable percentages and numbers of CD45^{high} leukocytes in the brains of control and ABX or GF mice. **a**, Gating strategy for T cells, B cells, dendritic cells (DCs) and macrophages (Mϕ) in the brain. **b**, Population frequencies and numbers of brain-resident CD45^{high} leukocytes in control and ABX mice. **c**, **d**, Population frequencies of CD4$^+$ T cells, CD8$^+$ T cells, CD19$^+$ B cells (**c**), CD11c$^+$ DCs and F4/80$^+$ macrophages (**d**) gated on brain-resident CD45^{high} leukocytes in control and ABX mice. **e**, Population frequencies and numbers of brain-resident CD45^{high} leukocytes in control and GF mice. **f**, **g**, Population frequencies of CD4$^+$ T cells, CD8$^+$ T cells, CD19$^+$ B cells (**f**), CD11c$^+$ DCs and F4/80$^+$ macrophages (**g**) gated on brain-resident CD45^{high} leukocytes in control and GF mice. **h**, Gating strategy of total myeloid cells and Ly6C^{high} monocytes in the brain. **i**, **j**, Population frequencies of total myeloid cells and Ly6C^{high} monocytes gated on brain-resident CD45^{high} leukocytes in control and ABX (**i**) or GF (**j**) mice. Data in **b**, **c**, **g**, **j** are representative of three independent experiments. $n = 4$ mice per group. Data in **d**, **i** are pooled from two independent experiments. $n = 8$ mice per group. Data in **e**, **f** are pooled from two independent experiments. $n = 6$ mice group. Data are mean ± s.e.m.; unpaired two-sided *t*-tests were used. *P* values are indicated on the figures. **k**, Fear extinction in control, GF and *Rag1*$^{-/-}$ mice in the single-session 30-tone fear extinction assay. Data are pooled from two independent experiments. Control $n = 18$, GF $n = 16$, *Rag1*$^{-/-}$ $n = 18$. Mean ± s.e.m.; AUC was calculated for each mouse within each group followed by one-way ANOVA with Tukey's multiple comparisons test. $F(2,49) = 8.558$, $P = 0.0006$. Adjusted *P* values are as follows: i = 0.0343, ii = 0.0004. **l**, Fear extinction of SPF-*Rag1*$^{-/-}$ and GF-*Rag1*$^{-/-}$ mice in the single-session 30-tone fear extinction assay. $n = 7$ mice per group. Mean ± s.e.m.; AUC was calculated for each mouse within each group followed by unpaired two-sided *t*-test between groups. *P* value is shown.

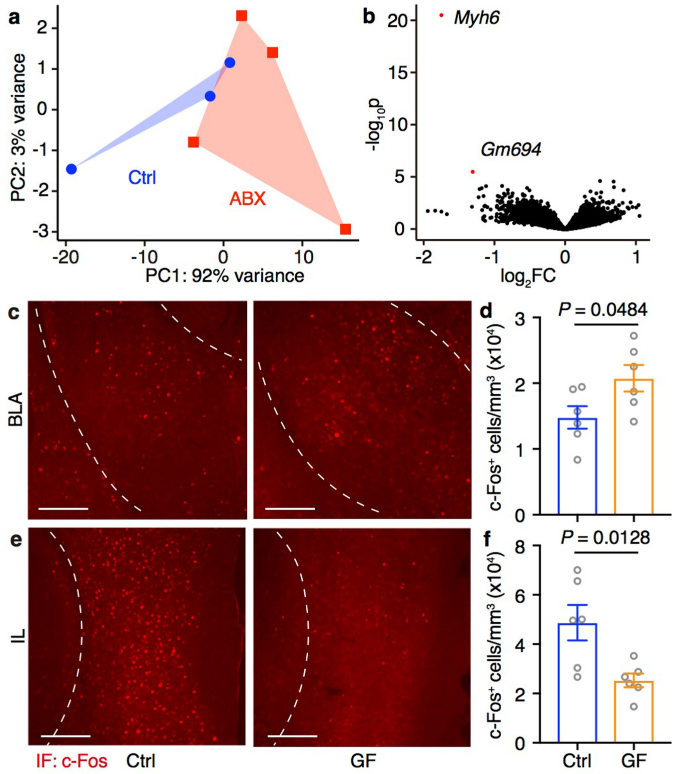

Extended Data Fig. 4 | Comparable transcriptomes of mPFCs dissected from control and ABX mice in the absence of fear conditioning and extinction. a, PCA of genome-wide transcriptional profiles of mouse mPFC in the absence of fear conditioning and extinction. Control $n = 3$, ABX $n = 4$. PERMANOVA test was used: $F = 2.52$, Df = 1, $P = 0.17$. **b**, Volcano plot of differential expression between control (negative $\log_2$FC) and ABX (positive $\log_2$FC) groups. DEGs (defined as FDR < 0.1, DESeq2 Wald test) are shown in red. **c**–**f**, Immunofluorescence staining of c-FOS (red) (**c**, **e**) and the density of c-FOS$^+$ neurons (**d**, **f**) in the BLA (**c**, **d**) or IL (**e**, **f**) of control and GF mice 90 min after classical fear extinction session 3. Data pooled from two independent experiments. $n = 6$ mice per group. Mean ± s.e.m.; unpaired two-sided t-tests. P values are shown. Scale bar, 200 μm.

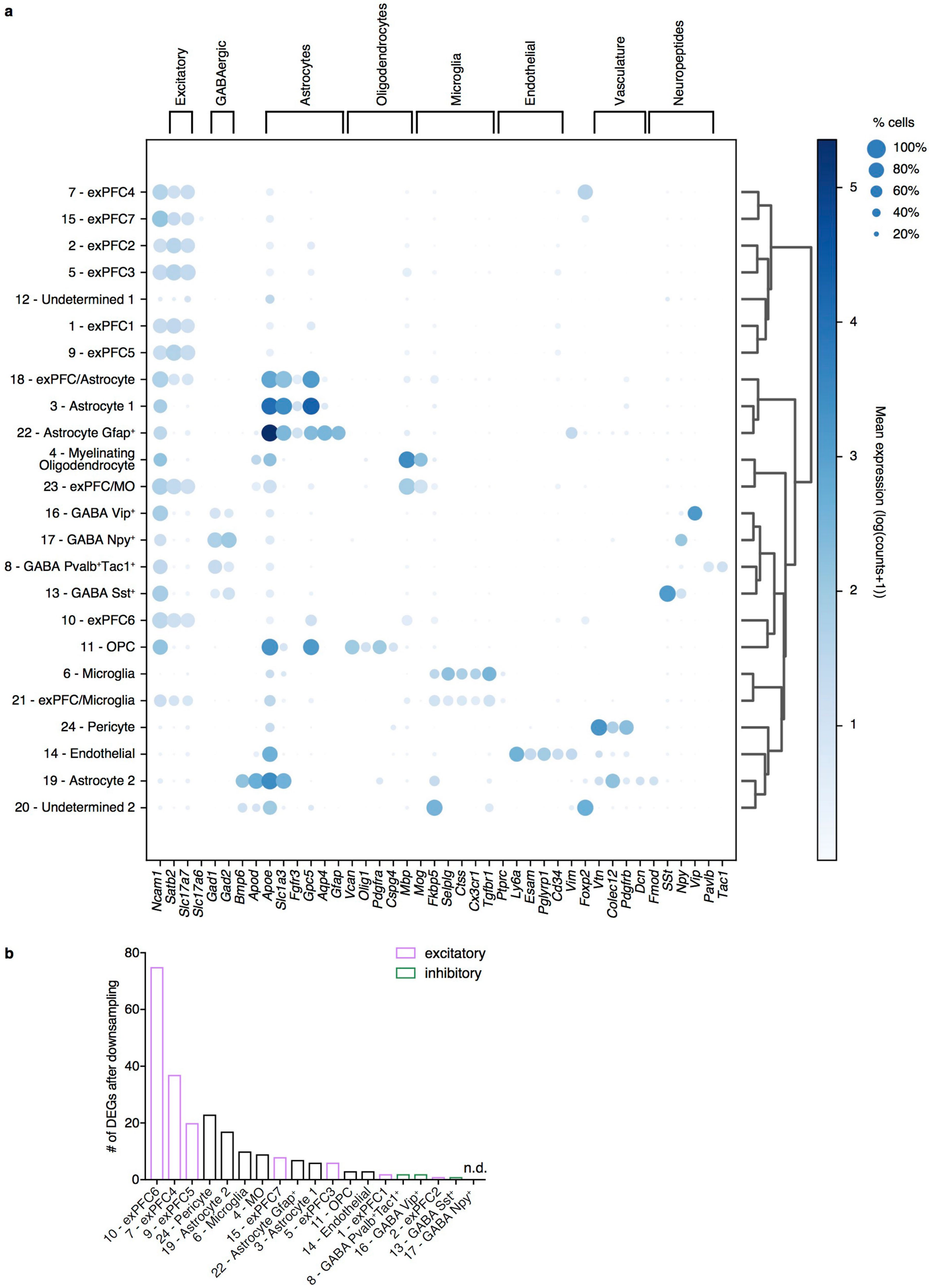

Extended Data Fig. 5 | Gene expression patterns of individual cell subsets in the mPFC. a, Proportion of expressing cells (dot size) and mean normalized expression of representative marker genes (columns) associated with the cell clusters shown in Fig. 2a (rows). Clusters are labelled with post facto annotation based on known marker genes. Ambiguous clusters expressing multiple canonical markers across cell types are annotated with both (for example, exPFC/astrocyte), and are likely to represent doublets. **b**, Number of significantly differentially expressed genes (*z*-test calculated on coefficients of mixed linear model, Bonferroni-corrected $P < 10^{-7}$) by cluster after downsampling each cluster to 500 nuclei, ranked from highest to lowest (clusters of doublets and undetermined annotations not included). exPFC, glutamatergic excitatory neurons from the PFC; GABA, γ-aminobutyric acid (GABA)ergic interneurons; OPC, oligodendrocyte progenitor cells; MO, myelinating oligodendrocytes.

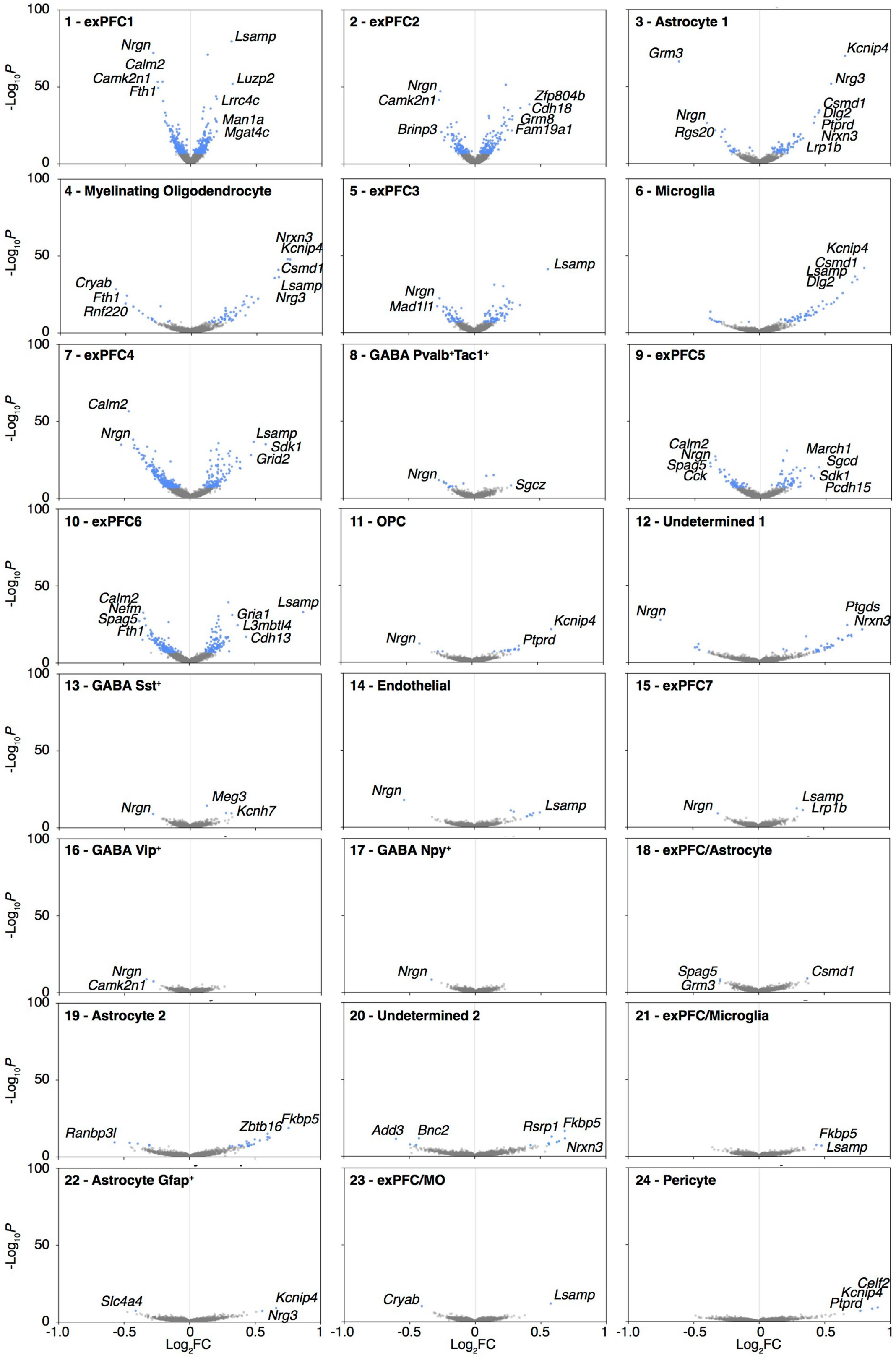

Extended Data Fig. 6 | Differential gene expression between control and ABX mice in individual clusters of mPFC cells. Differential expression of ABX versus control ($\log_2$FC) in each cluster in Fig. 2a and the associated significance. Blue, genes that are significantly differentially expressed (*z*-test calculated on coefficients of mixed linear model, Bonferroni-corrected $P < 10^{-7}$).

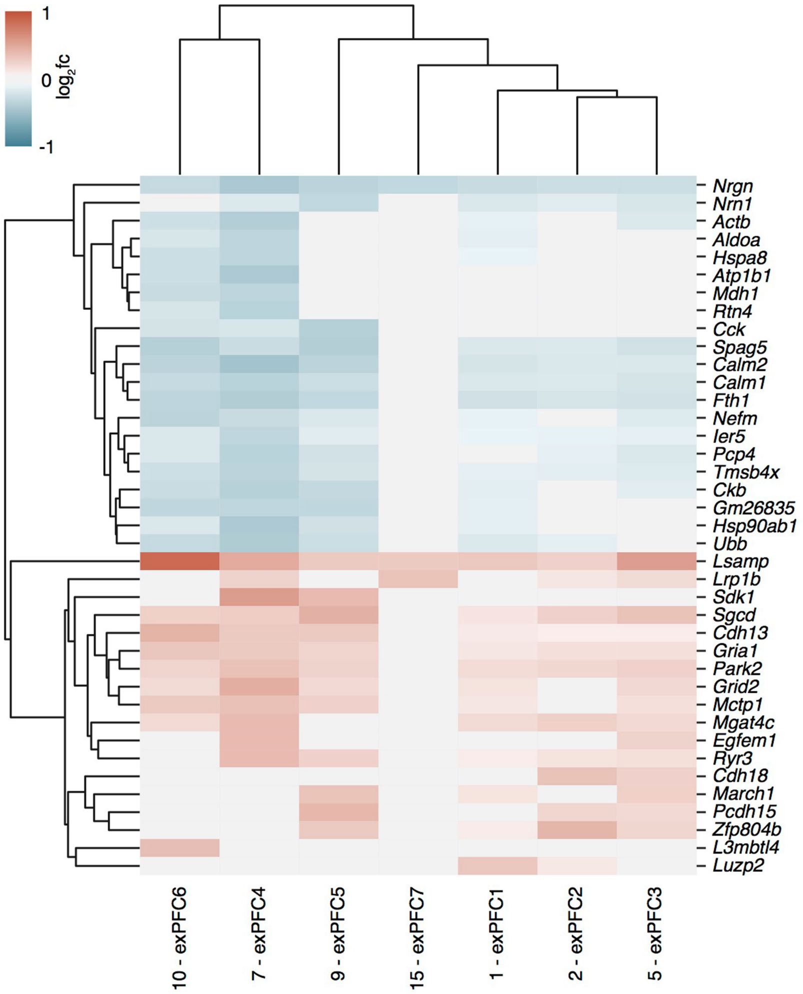

Extended Data Fig. 7 | Differentially expressed genes in ABX versus control mPFC samples shared by all excitatory neuronal subsets. Mean fold change in expression in excitatory neurons (columns) from Fig. 2a of genes (rows) that were significantly differentially expressed (*z*-test calculated on coefficients of mixed linear model, Bonferroni-corrected $P < 10^{-7}$) in at least 2 of these clusters, and with absolute $\log_2$FC ≥ 0.31 in at least 1 cluster.

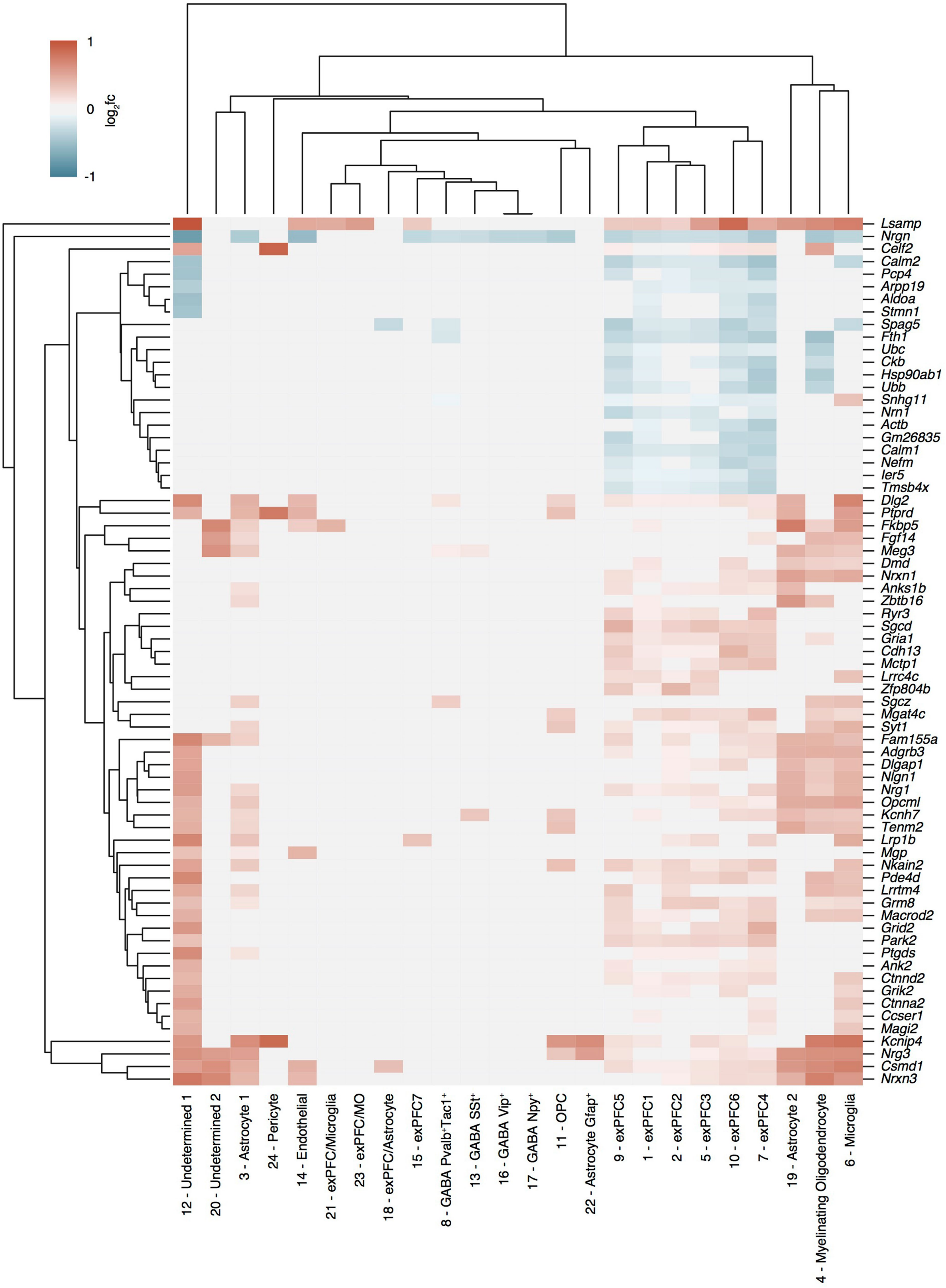

Extended Data Fig. 8 | Differentially expressed genes in ABX versus control mPFC samples shared by multiple cell types. Mean fold change in expression across all cell clusters (columns) from Fig. 2a of genes (rows) that were significantly differentially expressed (*z*-test calculated on coefficients of mixed linear model, Bonferroni-corrected $P < 10^{-7}$) in at least 4 clusters, and with absolute $\log_2$FC ≥ 0.31 in at least 1 cluster.

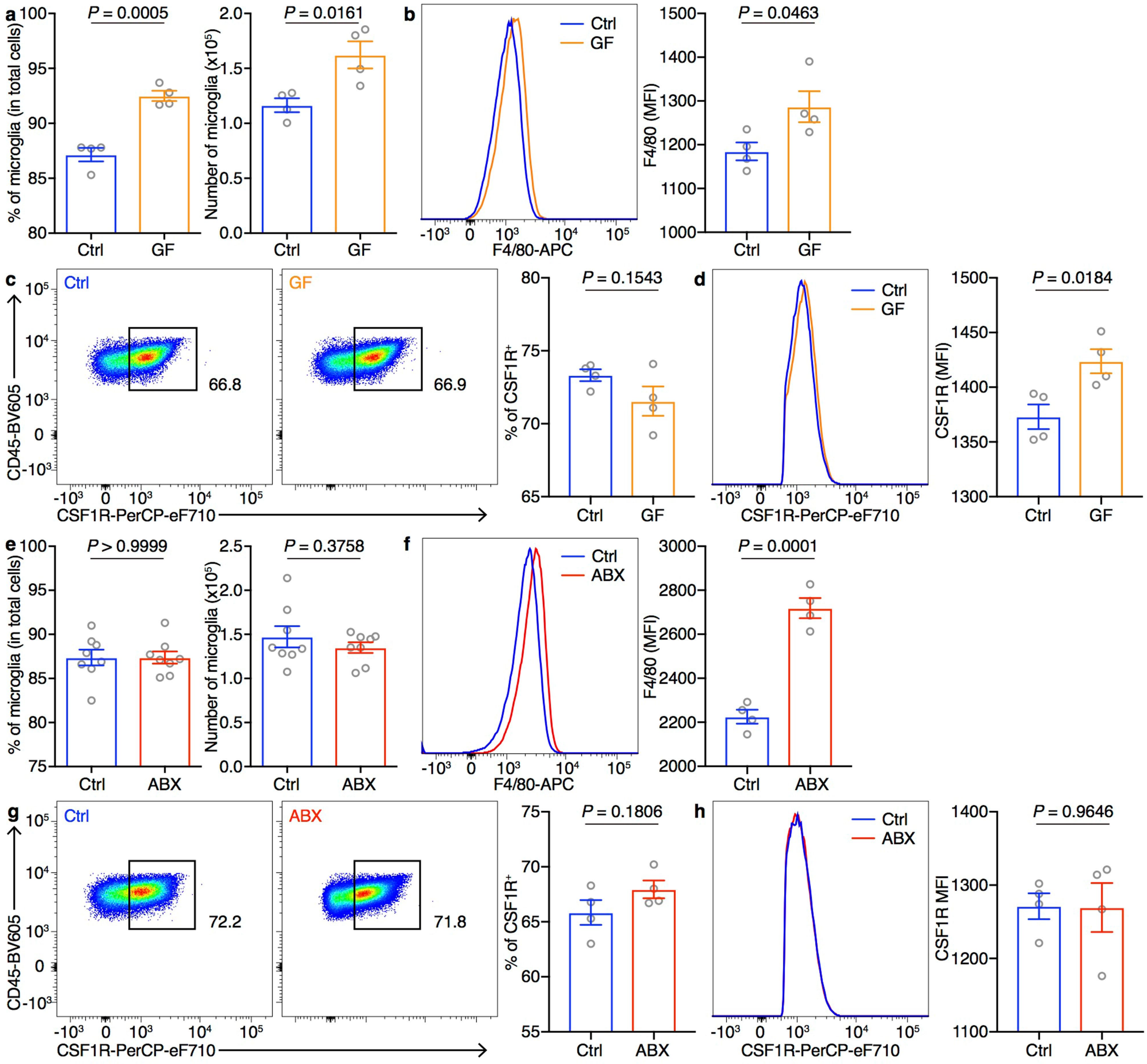

Extended Data Fig. 9 | Microglia in GF and ABX mice exhibit a developmentally immature phenotype. **a**, Population frequencies and numbers of microglia in control and GF mice. **b**, Representative flow cytometry histogram and mean fluorescence intensity (MFI) of F4/80 staining on microglia from control and GF mice. **c**, Representative flow cytometry plots and population frequencies of CSF1R$^+$ microglia in control and GF mice. **d**, Representative flow cytometry histogram and MFI of CSF1R expression gated on CSF1R$^+$ microglia from control and GF mice. Data in **a**–**d** are representative of three independent experiments, $n = 4$ mice per group. **e**, Population frequencies and numbers of microglia in control and ABX mice. **f**, Representative flow cytometry histogram and MFI of F4/80 staining on microglia from control and ABX mice. **g**, Representative flow cytometry plots and population frequencies of CSF1R$^+$ microglia in control and ABX mice. **h**, Representative flow cytometry histogram and MFI of CSF1R expression gated on CSF1R$^+$ microglia from control and ABX mice. Data in **e** are pooled from two independent experiments, $n = 8$ mice per group. Data in **f**–**h** are representative of two independent experiments, $n = 4$ mice per group. Mean ± s.e.m.; unpaired two-sided *t*-test. *P* values shown.

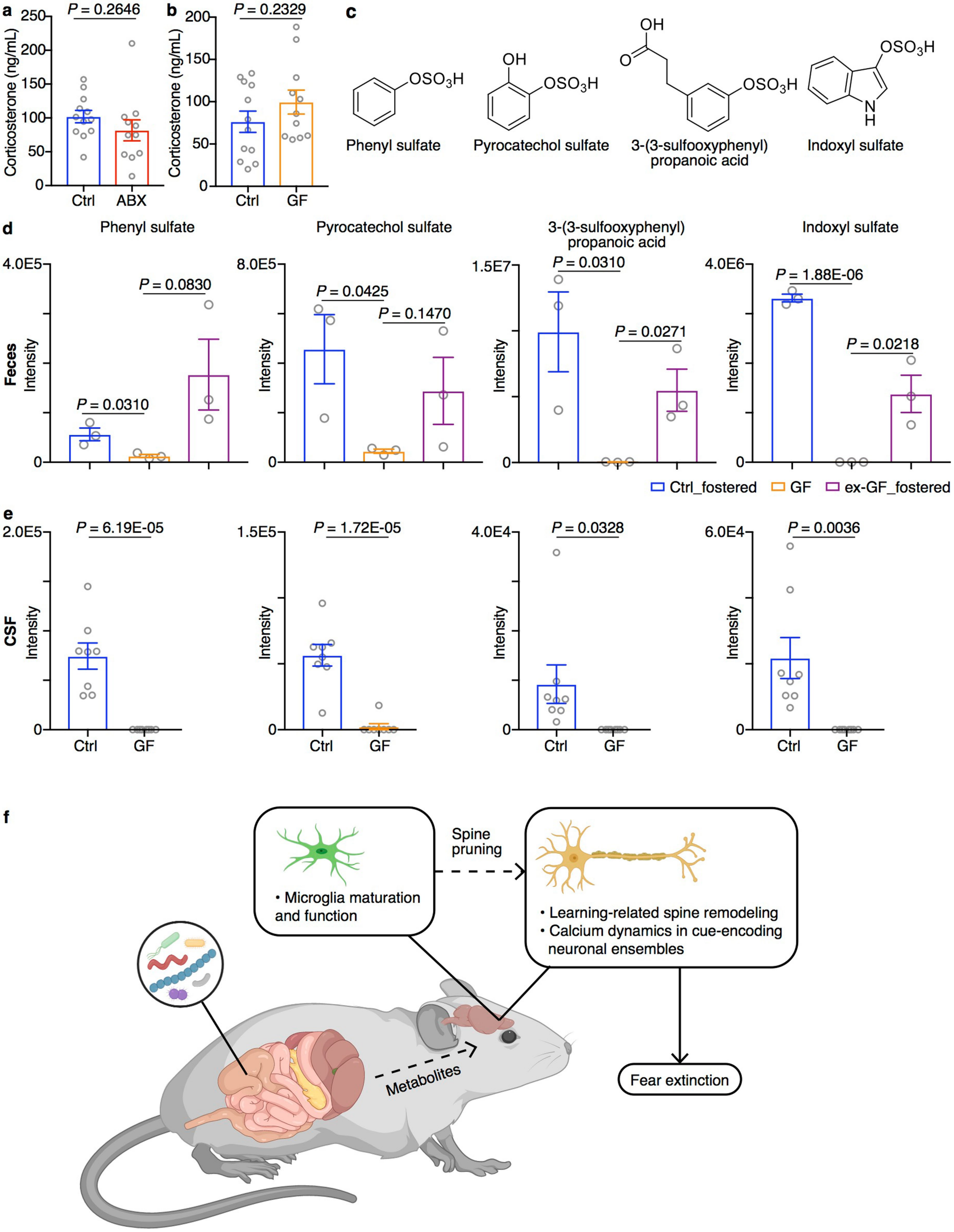

Extended Data Fig. 10 | Downregulation of metabolites in GF mice. **a**, Enzyme-linked immunosorbent assay (ELISA) quantification of plasma corticosterone in control and ABX mice. Data pooled from three independent experiments. Control *n* = 12; ABX *n* = 11. **b**, ELISA quantification of plasma corticosterone in control and GF mice. Data pooled from three independent experiments. Control *n* = 12; GF *n* = 11. Mean ± s.e.m. **c**, Structures of phenyl sulfate, pyrocatechol sulfate, 3-(3-sulfooxyphenyl)propanoic acid and indoxyl sulfate. **d**, Relative abundances of phenyl sulfate, pyrocatechol sulfate, 3-(3-sulfooxyphenyl)propanoic acid and indoxyl sulfate in faecal samples from Ctrl_fostered, GF and ex-GF_fostered mice as determined by LC–MS. *n* = 3 mice per group. **e**, Relative abundances of phenyl sulfate, pyrocatechol sulfate, 3-(3-sulfooxyphenyl)propanoic acid and indoxyl sulfate in CSF samples from control and GF mice as determined by LC–MS. Data are representative of two independent experiments, *n* = 8 mice per group. Mean ± s.e.m.; unpaired two-sided *t*-test. *P* values shown. **f**, Schematic of the microbiota–gut–brain axis in fear extinction learning. Our data inform a model in which alterations in the microbiota and their metabolites influence neuronal function and learning-related plasticity, which may be due to altered microglia-mediated synaptic pruning, and subsequently regulate fear extinction behaviour.

Corresponding author(s): David Artis, Conor Liston

Last updated by author(s): Aug 7, 2019

Reporting Summary

Nature Research wishes to improve the reproducibility of the work that we publish. This form provides structure for consistency and transparency in reporting. For further information on Nature Research policies, see Authors & Referees and the Editorial Policy Checklist.

Statistics

For all statistical analyses, confirm that the following items are present in the figure legend, table legend, main text, or Methods section.

n/a	Confirmed	
☐	☒	The exact sample size (n) for each experimental group/condition, given as a discrete number and unit of measurement
☐	☒	A statement on whether measurements were taken from distinct samples or whether the same sample was measured repeatedly
☐	☒	The statistical test(s) used AND whether they are one- or two-sided *Only common tests should be described solely by name; describe more complex techniques in the Methods section.*
☐	☒	A description of all covariates tested
☐	☒	A description of any assumptions or corrections, such as tests of normality and adjustment for multiple comparisons
☐	☒	A full description of the statistical parameters including central tendency (e.g. means) or other basic estimates (e.g. regression coefficient) AND variation (e.g. standard deviation) or associated estimates of uncertainty (e.g. confidence intervals)
☐	☒	For null hypothesis testing, the test statistic (e.g. F, t, r) with confidence intervals, effect sizes, degrees of freedom and P value noted *Give P values as exact values whenever suitable.*
☒	☐	For Bayesian analysis, information on the choice of priors and Markov chain Monte Carlo settings
☒	☐	For hierarchical and complex designs, identification of the appropriate level for tests and full reporting of outcomes
☐	☒	Estimates of effect sizes (e.g. Cohen's d, Pearson's r), indicating how they were calculated

Our web collection on statistics for biologists contains articles on many of the points above.

Software and code

Policy information about availability of computer code

Data collection	Graphic State v4.0, Stereo Investigator v9, FV31S, ZEN Black v2.6, BD FACSDiva v8.0.1, QuantStudio Real-Time PCR software v1.0
Data analysis	MATLAB R2015a, Prism 7, Fiji, Flowjo 10.4.0, Autotyping 15.04, Image Stabilizer Plugin for ImageJ, CASAVA v1.8.2, FLEXBAR v2.4, STAR v2.3.0, Rsubread, DESeq2 v1.18, vegan R package (https://CRAN.R-project.org/package=vegan), USEARCH v11, phyloseq R package, Cell Ranger v2.0, Scanpy v1.4.0, Louvain algorithm, Python, MSConvert, centWave XCMS algorithm

For manuscripts utilizing custom algorithms or software that are central to the research but not yet described in published literature, software must be made available to editors/reviewers. We strongly encourage code deposition in a community repository (e.g. GitHub). See the Nature Research guidelines for submitting code & software for further information.

Data

Policy information about availability of data

All manuscripts must include a data availability statement. This statement should provide the following information, where applicable:

- Accession codes, unique identifiers, or web links for publicly available datasets
- A list of figures that have associated raw data
- A description of any restrictions on data availability

RNA-seq data, 16S rRNA-seq data and single nucleus RNA-seq data are available at Gene Expression Omnibus and BioProject under accession number GSE134808, PRJNA556230 and GSE135326, respectively.

Field-specific reporting

Please select the one below that is the best fit for your research. If you are not sure, read the appropriate sections before making your selection.

☒ Life sciences ☐ Behavioural & social sciences ☐ Ecological, evolutionary & environmental sciences

For a reference copy of the document with all sections, see nature.com/documents/nr-reporting-summary-flat.pdf

Life sciences study design

All studies must disclose on these points even when the disclosure is negative.

Sample size	No statistical methods were used to predetermine sample size for experimentation. The sample size was estimated from preliminary experiments or from reports in the literature.
Data exclusions	Samples with significant drift during microscopy (i.e. tracked cells or regions that went out of focus or out of frame) were excluded from subsequent analysis. These exclusion criteria were not pre-established though are standard in live timelapse imaging studies.
Replication	Experiments were repeated with at least two to three biologically independent for all results presented in the manuscript. If the group size was small (due to limited availability of reagents or mouse strains), data from replicate experiments were pooled for graphical representation. All replicates are biological replicates obtained from biologically independent experiments.
Randomization	We did not use randomization to assign animals to experimental groups. As whenever possible littermate controls were used, age did not constitute a variable (and was matched for non-littermates).
Blinding	For dendritic spine imaging data analysis, raters blinded to experimental conditions. All other animal studies were not blinded since treatment and experimental analysis could not be separated, blinding of the investigators was not possible.

Reporting for specific materials, systems and methods

We require information from authors about some types of materials, experimental systems and methods used in many studies. Here, indicate whether each material, system or method listed is relevant to your study. If you are not sure if a list item applies to your research, read the appropriate section before selecting a response.

Materials & experimental systems

n/a	Involved in the study	
☐	☒	Antibodies
☒	☐	Eukaryotic cell lines
☒	☐	Palaeontology
☐	☒	Animals and other organisms
☒	☐	Human research participants
☒	☐	Clinical data

Methods

n/a	Involved in the study	
☒	☐	ChIP-seq
☐	☒	Flow cytometry
☒	☐	MRI-based neuroimaging

Antibodies

Antibodies used	The antibodies are described below. All antibodies were purchased from BD, eBioscience (Thermo Fisher), Biolegend, xxx. All antibodies were validated by manufacturers and in previous publications. Antibodies for flow cytometry: CD16/CD32 - clone 93 - purified - Biolegend - https://www.biolegend.com/en-us/products/purified-anti-mouse-cd16-32-antibody-190 CD45 - clone 30-F11 -BV605 - Biolegend - https://www.biolegend.com/en-us/products/brilliant-violet-605-anti-mouse-cd45-antibody-8721 CD4 - clone RM4-5 - FITC - eBioscience - https://www.thermofisher.com/antibody/product/CD4-Antibody-clone-RM4-5-Monoclonal/11-0042-82 CD8a - clone 53-6.7 - PE - biolegend - https://www.biolegend.com/en-us/products/pe-anti-mouse-cd8a-antibody-155 CD19 - clone 1D3 - PerCP-Cy5.5 - eBioscience - https://www.thermofisher.com/antibody/product/CD19-Antibody-clone-eBio1D3-1D3-Monoclonal/45-0193-82 CD11b - clone M1/70 - APC-eF780 - eBioscience - https://www.thermofisher.com/antibody/product/CD11b-Antibody-clone-M1-70-Monoclonal/47-0112-82 CD11c - clone N418 - APC-eF780 - eBioscience - https://www.thermofisher.com/antibody/product/CD11c-Antibody-clone-N418-Monoclonal/47-0114-82 F4/80 - clone BM8 - APC - eBioscience - https://www.thermofisher.com/antibody/product/F4-80-Antibody-clone-BM8-Monoclonal/17-4801-82 Ly6G - clone 1A8-Ly6g - PE - eBioscience - https://www.thermofisher.com/antibody/product/Ly-6G-Antibody-clone-1A8-Ly6g-

	Monoclonal/12-9668-82 Ly6C - clone HK1.4 - PE-Cy7 - eBioscience - https://www.thermofisher.com/antibody/product/Ly-6C-Antibody-clone-HK1-4-Monoclonal/25-5932-82 CSF1R - clone AFS98 - PerCP-eF710 - eBioscience - https://www.thermofisher.com/antibody/product/CD115-c-fms-Antibody-clone-AFS98-Monoclonal/46-1152-82 All flow antibodies were used at 1:200. Antibodies for immunofluorescence staining: c-Fos - clone 4 - Santa Cruz - https://www.scbt.com/scbt/product/c-fos-antibody-4 Synaptophysin - clone SVP-38 - Sigma - https://www.sigmaaldrich.com/catalog/product/sigma/sab4200544?lang=en&region=US PSD-95 - clone 7E3-1B8 - Sigma - https://www.sigmaaldrich.com/catalog/product/mm/cp35?lang=en&region=US The above three antibodies were used at 1:1,000. Donkey anti-Rabbit IgG (H+L) - AF555 - https://www.thermofisher.com/antibody/product/Donkey-anti-Rabbit-IgG-H-L-Highly-Cross-Adsorbed-Secondary-Antibody-Polyclonal/A-31572 Donkey anti-Mouse IgG (H+L) - AF555 - https://www.thermofisher.com/antibody/product/Donkey-anti-Mouse-IgG-H-L-Highly-Cross-Adsorbed-Secondary-Antibody-Polyclonal/A-31570 The above two secondary antibodies were used at 1:500. All antibodies information (including catalog number) could be easily found via the vendor websites.
Validation	All antibodies are commercially available and validated by the manufacturer. Vendor websites for antibodies were listed above and the validations can be found there.

Animals and other organisms

Policy information about studies involving animals; ARRIVE guidelines recommended for reporting animal research

Laboratory animals	C57BL/6J (Jax 664), Rag1-/- (Jax 2216), Thy1-YFP-H (Jax 3782) and BALB/c (Jax 651) mice were purchased from The Jackson Laboratory and bred in-house. Male mice were used at 7-16 weeks of age. In individual experiments, all animals were age-matched. All mice were maintained under specific pathogen-free (SPF) conditions on a 12-hour light/dark cycle, and provided food and water ad libitum. Germ-free C57BL/6 mice and gnotobiotic mice were maintained at Weill Cornell Medical College, New York.
Wild animals	No wild animals included.
Field-collected samples	No field-collected samples included.
Ethics oversight	All protocols were approved by the Weill Cornell Medicine Institutional Animal Care and Use Committees (IACUC), and all mice were used in accordance of governmental and institutional guidelines for animal welfare.

Note that full information on the approval of the study protocol must also be provided in the manuscript.

Flow Cytometry

Plots

Confirm that:

☒ The axis labels state the marker and fluorochrome used (e.g. CD4-FITC).

☒ The axis scales are clearly visible. Include numbers along axes only for bottom left plot of group (a 'group' is an analysis of identical markers).

☒ All plots are contour plots with outliers or pseudocolor plots.

☒ A numerical value for number of cells or percentage (with statistics) is provided.

Methodology

Sample preparation	Sample preparation is described in methods in the 'Brain-resident immune cell isolation and flow cytometry' section.
Instrument	A custom configuration Fortessa flow cytometer (BD Biosciences).
Software	FACS DIVA software (BD Biosciences) and FlowJo V10 (Tree Star).
Cell population abundance	No cell sorting is performed.
Gating strategy	The gating strategy is presented in Extended Data Fig. 3 and Extended Data Fig. 9.

☒ Tick this box to confirm that a figure exemplifying the gating strategy is provided in the Supplementary Information.